minerals

MDPI

Article

Geochronology and Geochemistry of Paleoproterozoic Mafic Rocks in Northern Liaoning and Their Geological Significance

Jingsheng Chen [1,2], Yi Tian [3], Zhonghui Gao [4], Bin Li [1,2,*], Chen Zhao [1,2], Weiwei Li [4], Chao Zhang [1,2] and Yan Wang [1,2]

[1] Shenyang Geological Survey Center of China Geological Survey, Shenyang 110034, China; jschen0712@126.com (J.C.); aaron198807@163.com (C.Z.); congray@163.com (C.Z.); wangy68413@163.com (Y.W.)
[2] Northeast Geological S&T Innovation Center of China Geological Survey, Shenyang 110034, China
[3] Liaoning Geological and Mineral Survey Institute Co., Ltd., Shenyang 110031, China; lnsytianyi@163.com
[4] Institute of Geology and Mineral Resources of Liaoning Co., Ltd., Shenyang 110029, China; 13897938707@163.com (Z.G.); 15040028747@163.com (W.L.)
* Correspondence: libin@mail.cgs.gov.cn

Abstract: Petrological, geochronological, and geochemical analyses of mafic rocks in northern Liaoning were conducted to constrain the formation age of the Proterozoic strata, and to further study the source characteristics, genesis, and tectonic setting. The mafic rocks in northern Liaoning primarily consist of basalt, diabase, gabbro, and amphibolite. Results of zircon U-Pb chronology reveal four stages of mafic magma activities in northern Liaoning: the first stage of basalt (2209 ± 12 Ma), the second stage of diabase (2154 ± 15 Ma), the third stage of gabbro (2063 ± 7 Ma), and the fourth stage of magmatic protolith of amphibolite (2018 ± 13 Ma). Combined with the unconformity overlying Neoproterozoic granite, the formation age of the Proterozoic strata in northern Liaoning was found to be Paleoproterozoic rather than Middle Neoproterozoic by the geochronology of these mafic rocks. A chronological framework of mafic magmatic activities in the eastern segment of the North China Craton (NCC) is proposed. The mafic rocks in northern Liaoning exhibit compositional ranges of 46.39–50.33 wt% for SiO_2, 2.95–5.08 wt% for total alkalis ($K_2O + Na_2O$), 6.17–7.50 wt% for MgO, and 43.32–52.02 for the Mg number. TiO_2 contents lie between 1.61 and 2.39 wt%, and those of MnO between 0.17 and 0.21 wt%. The first basalt and the fourth amphibolite show low total rare earth element contents. Normalized against primitive mantle, they are enriched in large ion lithophile elements (Rb, Ba, K), depleted in high field strength elements (Th, U, Nb, Ta, Zr, Ti), and exhibit negative anomalies in Sr and P, as well as slight positive anomalies in Zr and Hf. The second diabase and the third gabbro have similar average total rare earth element contents. The diabase shows slight negative Eu anomalies (Eu/Eu* = 0.72–0.88), enrichment in large ion lithophile elements (Ba), depletion in Rb, and slight positive anomalies in high field strength elements (Th, U, Nb, Ta, Zr, Hf, Ti), with negative anomalies in K, Sr, and P. The gabbro is enriched in large ion lithophile elements (Rb, Ba, K), depleted in high field strength elements (Th, U, Nb, Ta, Zr, Hf), and exhibits positive anomalies in Eu (Eu/Eu* = 1.31–1.37). The contents of Cr, Co, and Ni of these four stages of mafic rocks are higher than those of N-MORB. The characteristics of trace element ratios indicate that the mafic rocks belong to the calc-alkaline series and originate from the transitional mantle. During the process of magma ascent and emplacement, it is contaminated by continental crustal materials. There are residual hornblende and spinel in the magma source of the first basalt. The other three magma sources contain residual garnet and spinel. The third gabbro was formed in an island arc environment, and the other three stages of mafic rocks originated from the Dupal OIB and were formed in an oceanic island environment. The discovery of mafic rocks in northern Liaoning suggests that the Longgang Block underwent oceanic subduction and extinction in both the north and south in the Paleoproterozoic, indicating the possibility of being in two different tectonic domains.

Citation: Chen, J.; Tian, Y.; Gao, Z.; Li, B.; Zhao, C.; Li, W.; Zhang, C.; Wang, Y. Geochronology and Geochemistry of Paleoproterozoic Mafic Rocks in Northern Liaoning and Their Geological Significance. *Minerals* **2024**, *14*, 717. https://doi.org/10.3390/min14070717

Academic Editors: Federica Zaccarini and Giorgio Garuti

Received: 5 May 2024
Revised: 14 July 2024
Accepted: 15 July 2024
Published: 16 July 2024

Keywords: Paleoproterozoic mafic rocks; zircon U-Pb chronology; geochemistry; feature of source; tectonic setting

1. Introduction

As one of the oldest cratons in the world, the North China Craton (NCC) is a product of the amalgamation of multiple micro landmasses during the Late Neoarchean to Paleoproterozoic [1–7]. The researchers have different explanations on the tectonic evolution of the NCC. Four Archean landmasses and three Paleoproterozoic orogenic belts have been identified by some researchers (Figure 1c; [1,2,7]), and the aggregation process is summarized as follows: (1) In the western part of the NCC, the Yinshan Block and the Ordos Block converged along the Khondalite Belt at 1.95 Ga, forming a unified land block known as the Western Block. (2) In the eastern part, the Longgang Block and the Liaonan–Rangnim Block converged along the Jiao-Liao-Ji Belt (JLJB) at 1.92 Ga resulting in the formation of the Eastern Block. (3) The final collision occurred at 1.85 Ga between the Eastern and Western Blocks along the Trans-Central Orogenic Belt, leading to the final amalgamation of the NCC into a unified Precambrian continent [1,2,7]. However, other scholars have a different understanding of the convergence process of the NCC, with regard to the amalgamation of smaller tectonic units into larger continental landmasses at the end of the Archean and into the Paleoproterozoic with the formation of the Columbia Continent [3,4]. The Western Block collided with the arc-modified margin of the composite Eastern Block at 2.43 Ga leading to the formation of the Central Orogenic Belt with the imbricated arc and fore-arc ophiolitic mélanges. The northern margin of the craton was modified to become an Andean-style arc from 2.3 Ga to 1.9 Ga soon after this collision, and numerous magmatic rocks, volcanic and volcaniclastic rocks, and thick clastic sediments occurred in the continental-margin arc and retro-arc foreland basins. From about 1.88 to 1.79 Ga, the Columbia/Nuna Continent collided with the NCC along the northern margin of the craton resulting in the formation of the Inner Mongolia–Northern Hebei Orogen (IMNHO) [3,4,8,9]. Thus, the Paleoproterozoic geological bodies exposed within the orogenic belt are the key to reconstructing the tectonic evolution of the NCC.

In the eastern segment of the NCC, the well-known Paleoproterozoic JLJB is composed of a large amount of Paleoproterozoic magmatic, sedimentary, and metamorphic rocks, and has been studied extensively [1,2,10–20]. As the focus of debate, four primary tectonic evolution models of the JLJB have been proposed by researchers including: (1) the opening and closing of a Paleoproterozoic intracontinental rift [21–23]; (2) the collision of a continent–arc–continent system [24–27]; (3) a complete Wilson cycle encompassing Paleoproterozoic rifting–extension–ocean basin–subduction–collision [2,6,7,28,29]; and (4) the opening and closing of a back-arc basin [10,13–15] or retro-arc foreland basin [4,5,8]. Large-scale Paleoproterozoic mafic dykes developed in the JLJB [13,14], and they are direct carriers reflecting the stages of magmatic activity, the characteristics of magma source, and the tectonic setting. The study of these rocks provides valuable insights into the composition and behavior of the Earth's interior. Thus, the mafic rocks in the JLJB are the key to discussing the evolution of the tectonic belt.

In addition to the JLJB, many Paleoproterozoic magmatic and metamorphic events have been identified in the Qingyuan terrane of the northern margin of the NCC [30–32]. The Paleoproterozoic Inner Mongolia–Northern Hebei Orogen, as defined by Kusky et al. (2007), has been extended to the northern Liaoning but lacks direct geochronological evidence [4,5,9]. A suite of low-grade metamorphic rocks consisting of dolomite, sandstone, and siltstone has been exposed in northern Liaoning. Due to a lack of direct evidence of geochronology, its deposition age has been controversial, and it is temporarily classified as Mesoproterozoic based solely on lithological comparisons [33]. Large-scale mafic rocks intrude into this stratigraphic sequence. According to whole-rock K–Ar dating results, these mafic rocks are considered to have formed in the Early Triassic [33]. However,

during the field investigation, the authors found that these mafic rocks intrude into the dolomite, or are enveloped by marble, and have undergone high erosion, alteration, and metamorphism, similar to the large-scale Paleoproterozoic mafic dykes developed in the Liaoyang–Haicheng area in the south of the Longgang Block, rather than the Mesozoic mafic dykes [13,14]. Meanwhile, a 2.12 Ga metabasic dyke has recently been reported in Qingyuan [30]. Therefore, are the mafic rocks in northern Liaoning also products of the Paleoproterozoic magmatic events? What is the relationship with the mafic rocks in the JLJB and the tectonic setting in which they were formed? The composition of mafic–ultramafic rocks can directly reflect their sources and tectonic settings. Thus, the mafic rocks in northern Liaoning were selected for petrographic, geochronological, and geochemical studies to constrain the deposition age of the Proterozoic sediments and reconstruct the Paleoproterozoic tectonic evolution in this area.

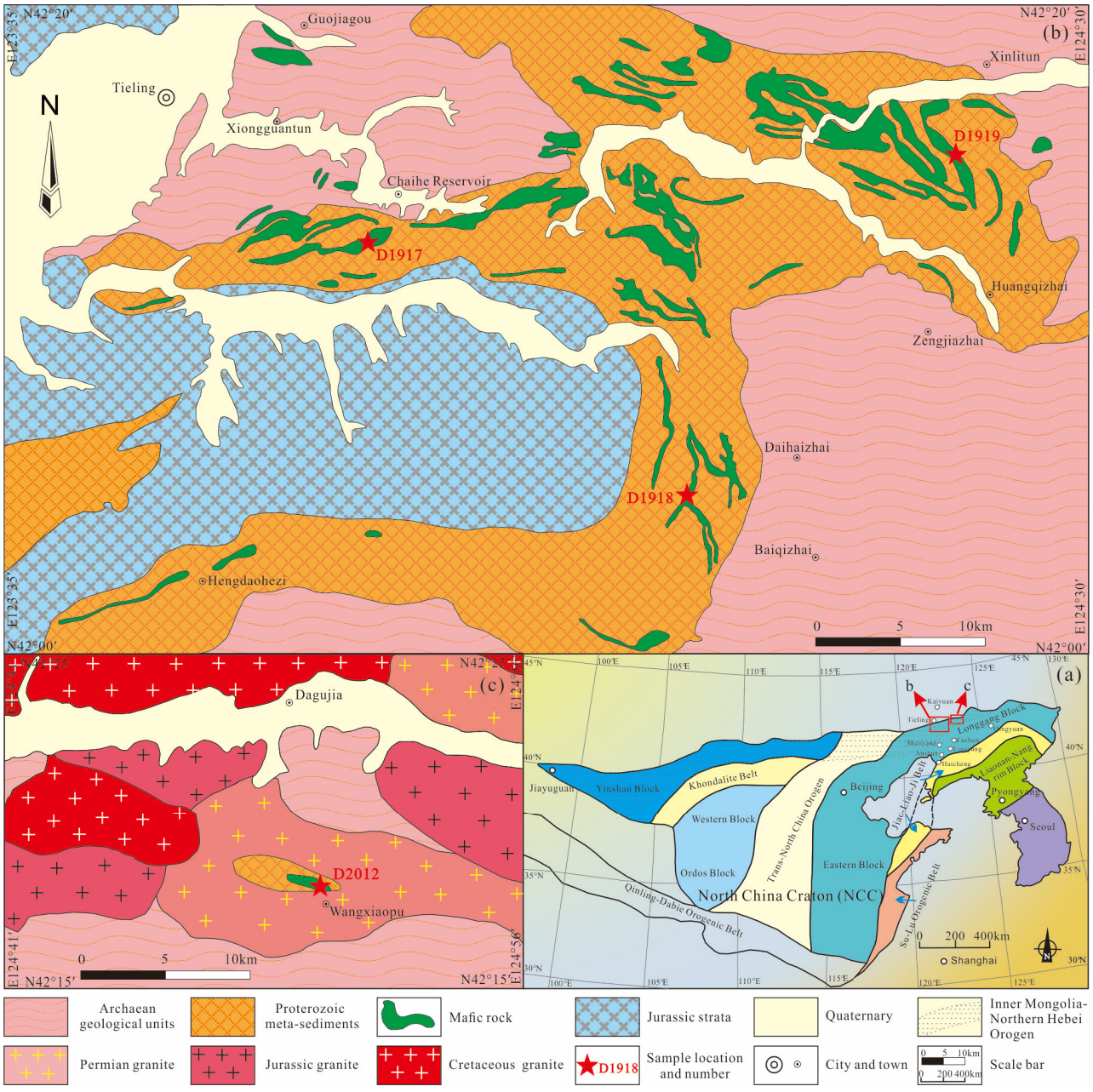

Figure 1. The tectonic location (**a**) (modified after Zhao, 2005 [1]); simplified geological map and sample location (**b**,**c**).

2. Geological Setting and Sample Descriptions

2.1. Geological Setting

The Precambrian basement of Liaodong Peninsula, located in the northeastern segment of the NCC, is composed of the Archean crystalline basement including the Liaonan–Nangrim Block in the southeast and the Longgang Block in the northwest, and the Paleoproterozoic JLJB in the center (Figure 1a; [1]). Archean to Paleoproterozoic supracrustal and granitoid rocks are exposed in the Liaonan–Nangrim Block in the southern Liaoning [34]. The Paleoproterozoic JLJB between these two blocks mainly contains metavolcano-sedimentary successions and granitic to mafic intrusions that were metamorphosed to greenschist–amphibolite facies [13–20]. The Longgang Block in the northern Liaoning exhibits extensive occurrences of tonalite–trondhjemite–granodiorite rocks (TTGs) [35–37] and basic volcanic rock [38]. These rocks, which date back approximately 3.8 Ga, have been discovered in the Anshan area. Furthermore, various zircons of magmatic, xenocrystal, and detrital origins, with ages $\geq$ 3.0 Ga, have been identified in this region [39].

The Proterozoic geological units are mainly exposed in the northern Liaoning, located from north of Shenyang–Fushun to Kaiyuan, and from Tieling to Wangxiaopu in the east. Based on rock composition, the stratigraphy is compared with the Changcheng and Jixian Systems' strata in western Liaoning, and is placed in the Mesoproterozoic. According to the current classification scheme, it is divided from bottom to top into the Daposhan Formation, Kangzhuangzi Formation, and Guanmenshan Formation of the Changcheng System, the Tongjiajie Formation, Hutouling Formation, Erdaogou Formation, Shimen Formation, and Yangshitun Formation of the Jixian System, the Yubeigou Formation and Yaomotaichong Formation of Neoproterozoic, and the Yintun Formation of the Nanhua System. These strata have undergone low-grade metamorphism and overlaid Archean gneiss with angular unconformity [33].

Large-scale mafic rocks as sills or dykes are widely distributed in northern Liaoning, generally trending east–west, and intruding into the Kangzhuangzi Formation, Guanmenshan Formation, Tongjiajie Formation, and Hutouling Formation with minor mafic intrusions into Neoarchean gneiss (Figure 1b). These mafic rocks can be subdivided into two belts: the northern belt extends from Guojia Gou to Xinlitun, and the southern belt extends from Chaihe Reservoir to Zengjiazhai. Additionally, sporadic outcrops of mafic rocks can be observed in the Xiongguantun area of Tieling City. They exhibit obvious contact metamorphic belt and chilled margins, with varying widths and abundant country rock xenoliths. The Precambrian basement in this area is covered by the Jurassic Qianwanling Formation, Nankangzhuang Formation, and Yingshugou Formation with unconformity (Figure 1b). Furthermore, through the 1:50,000 regional geological survey, a suite of two-mica schist, marble, and basalt (partially pillow-shaped) rock assemblage was identified in Wangxiaopu Village, which is in fault contact with the surrounding Permian granite and is intruded by later quartz veins (Figure 1c).

2.2. Petrological Characteristics of Mafic Rocks

In this study, 4 geochronological samples and 28 geochemical samples were collected from the intrusions of diabase, gabbro sills, and basalt associated with marble in the Proterozoic strata for analysis, respectively. The sampling locations are shown in Figure 1 and Table 1.

Sample D1917, basalt, was collected from 500 m south of Yunpangou Village, Xiongguantun Town (Figure 1b). It crops out as a pillow structure, with a fine-grained contact margin between the pillows (Figure 2a), and intrudes into the Guanmenshan Formation. It is black to grey in color with a porphyritic texture, massive structure, and a matrix of microcrystalline texture (Figure 2b,c). The phenocrysts are composed of plagioclase (~5%) and pyroxene (~5%). Plagioclase, subhedral to euhedral columnar crystals ranging from 0.5–2 mm in diameter, has undergone chloritization, epidotization, and calcitization. Pyroxene, euhedral columnar crystals, with a particle size of 0.5–2 mm, has undergone alteration into amphibole and carbonation. The matrix consists of microcrystalline plagioclase (~55%)

and pyroxene (~30%). Plagioclase is crystallized in subhedral columns with a particle size of 0.2–0.5 mm. Pyroxenes exhibit xenomorphic granular textures with a particle size of less than 0.2 mm. The accessory minerals are magnetite, apatite, etc., and the alteration minerals include chlorite, epidote, calcite, etc. (Figure 2c).

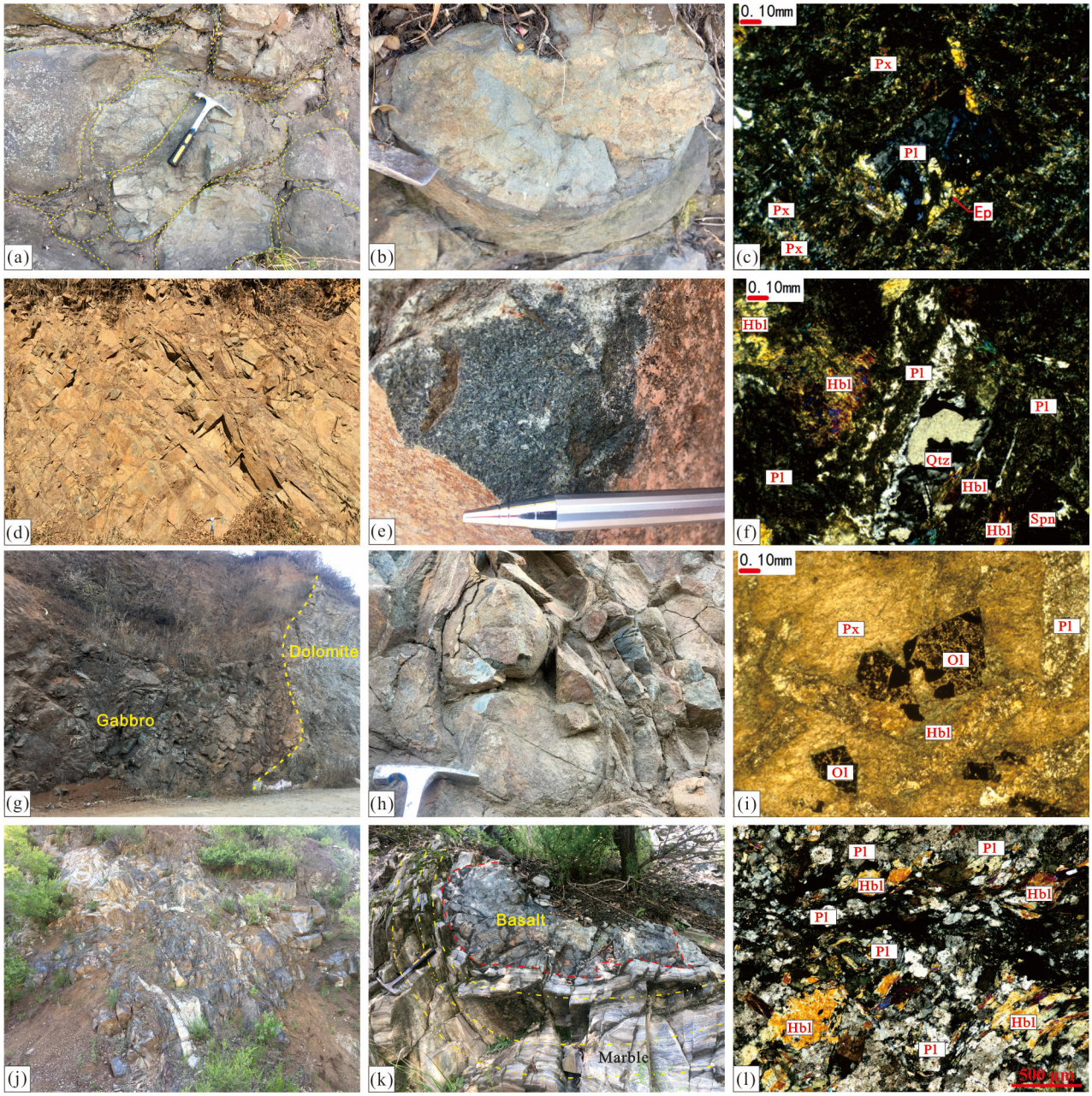

Figure 2. Occurrence and micro-pictures of mafic rocks from northern Liaoning. (**a**,**b**,**c**): D1917 basalt; (**a**): pillow-shaped basalt; (**b**): edge and center phases of pillow-shaped basalt; (**c**): microscopic characteristics of basalt; (**d**–**f**): D1918 diabase; (**d**): field occurrence of diabase dyke; (**e**): specimen of diabase; (**f**): microscopic characteristics of diabase; (**g**–**i**): D1919 gabbro; (**g**): gabbro intruded into marble; (**h**): spherical weathering of gabbro; (**i**): microscopic characteristics of gabbro; (**j**–**l**): D2012 amphibolite; (**j**): field occurrence of amphibolite; (**k**): amphibolite wrapped in marble in a pillow shape; (**l**): microscopic characteristics of amphibolite; Pl: plagioclase; Px: pyroxene; Ol: olivine; Hbl: hornblende; Spn: sphene; Ep: epidote.

Table 1. Location and lithology for the magmatic rocks from the Kaiyuan Area, North Liaoning.

Sample	GPS Location	Lithology	Results (Ma)
D1917	125°57′05.27″, 41°21′16.88″	Basalt	2154 ± 15
D1918	124°12′36.40″, 42°05′01.27″	Diabase	2209 ± 12
D1919	124°13′57.47″, 42°14′18.33″	Gabbro	2063 ± 7
D2012	124°51′44.51″, 42°19′09.73″	Amphibolite	2018 ± 13

Sample D1918, diabase, collected from northwest of Baiqizhai Town (Figure 1b), intrudes into the dolomite of the Guanmenshan Formation (Figure 2d) with a subhedral granular texture and massive structure (Figure 2e). The mineral components of the diabase are plagioclase (~55%), hornblende (~35%), biotite (~5%), and quartz (~3%) (Figure 2f). Plagioclase, with a subhedral columnar texture, and a polysynthetic twin, with a particle size of 0.5–2 mm and some particles of 2–3 mm, exhibits varying degrees of epidotization and zoidization. Hornblende occurs as brown–green, subhedral columnar crystals ranging from 0.2 to 2 mm in diameter, fading to light green hornblende in varying degrees. Biotite is brown, idiomorphic flaky, with a particle size of 0.2–2 mm, and exhibits varying degrees of chloritization showing a pseudomorphic or residual structure. Xenomorphic crystals of quartz fill interstices between plagioclase and hornblende grains with a particle size of <0.2 mm. Accessory minerals include magnetite, apatite, and sphene (Spn), with a content of about 2%. Alteration includes sericitization, chloritization, and epidotization (Figure 2f).

Sample D1919, gabbro, collected from north of Huangqizhai Town (Figure 1b), intrudes into dolomite (Figure 2g,h). It shows a gabbroic texture, an embedded olivine texture, and a massive structure (Figure 2i), and consists of plagioclase (~55%), pyroxene (~30%), olivine (~8%), hornblende (~5%), and biotite (~2%). Plagioclase shows a subhedral columnar texture and a polysynthetic twin, with a main particle size of 0.2–2 mm and some particles of 2–5 mm and 5–8 mm, and exhibits zoisitization. Pyroxene, subhedral columnar crystals ranging from 0.2 to 2 mm in diameter, shows an embedded olivine texture containing granular olivine, and partially shows brown amphibole reaction edges. Olivine, with a xenomorphic granular texture and a particle size of 0.1–0.5 mm, is strongly altered to serpentine, microscale biotite, magnetite, etc., retaining its structure. Colorless to green hornblende, xenomorphic to granular in shape, shows amphibole cleavage with a particle size of 0.2–0.5 mm, and has undergone varying degrees of chloritization. Biotite is brown, idiomorphic flaky, with a particle size of 0.2–0.5 mm. The accessory minerals are magnetite, ilmenite, etc. (Figure 2i).

Sample D2012, amphibolite, collected from the north of Wangxiaobao Village (Figure 1c), intruded by later felsic veins (Figure 2j), was wrapped in marble in a pillow shape in the field (Figure 2k), which displayed as the rock assemblage of oceanic islands. It is composed of primary minerals such as hornblende (~77%), plagioclase (~12%), and quartz (~6%) exhibiting a fine granular texture, columnar recrystallization texture, and gneissic structure (Figure 2l). Gray to green hornblende crystallizes as long columns with a particle size ranging from 0.05 to 85 mm. Plagioclase, subhedral-xenomorphic plate-columnar-shaped, with a particle size of 0.12–0.50 mm, shows obvious sericitization and clayification with polysynthetic twin partially. Quartz, with a xenomorphic granular texture and a particle size of 0.04–0.30 mm, shows a wavy extinction. A large amount of opaque dark minerals are distributed in ribbons and clumps, with a total content of about 5%. Alteration includes chloritization and epidotization (Figure 2l).

2.3. Zircons in These Mafic Rocks

Commonly, some researchers contend that zircons are exclusively observed in felsic rocks due to the gradual saturation of Zr (and Si) during magma evolution. Conversely, the origin of zircons from mafic rocks, particularly fine-grained basalt and diabase, is considered highly improbable [40,41]. However, in recent research, some researchers believe that zircon crystallization in low-Zr mafic magmas is possible [42]. They explored that possibility using 2D finite elements to model the crystallization of MORB melts confined in pores, and found that zircon-saturated volumes may form locally at the growing mineral–melt interfaces if the growth rate of a low Kd^{Zr} mineral (<0.2) is much faster than the diffusion rate of the rejected Zr^{4+} away into the melt, thus leading to the precipitation of zircon in low-Zr mafic magmas. Thus, zircon crystallization in low-Zr mafic magmas is perfectly possible under confined crystallization [42]. Through microscopic identification, zircons were identified in thin sections of these four mafic rocks. The micrographs are as follows (Figure 3).

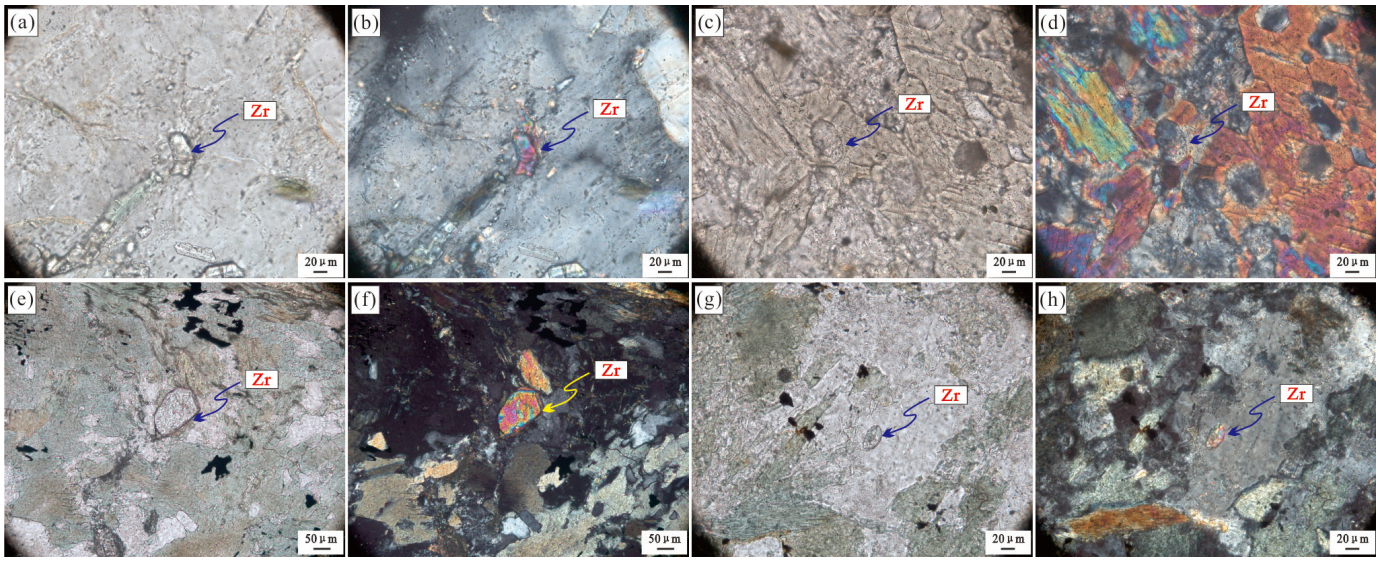

Figure 3. Micro-pictures of zircons in the mafic rocks from northern Liaoning. (**a**,**b**): D1917 zircon in pillow-shaped basalt; (**c**,**d**): D1918 zircon in diabase; (**e**,**f**): D1919 zircon in gabbro; (**g**,**h**): D2012 zircon in amphibolite; Zr: zircon.

3. Analytical Methods

3.1. Sample Preparation

Samples for geochronological analyses were first cleaned, crushed, and ground after being collected from the field. The zircon crystals were then separated from these samples using conventional heavy liquid and magnetic techniques at Langfang Yuneng Mineral Separation Co., Ltd. in Langfang, China. The separated zircons were carefully hand-picked under a binocular microscope. To examine their internal structures, the selected zircons were embedded in epoxy resin, polished, and imaged using a scanning electron microscope with cathodoluminescence (CL) at the Beijing Gaonian Navigation Technology Limited Company in Beijing, China. CL images of four samples were obtained using a CAMECA SX51 microprobe (CAMRCA, Gennevilliers, France), operating at 50 kv and 15 nA.

3.2. Zircon LA-ICP-MS U-Pb Isotope Dating

The LA-ICP-MS U-Pb isotope analyses were performed using an Agilent 7500a (Agilent Technologies Co., Ltd, Santa Clara, CA, USA) quadrupole ICP-MS with a UP-193 Solid-State Laser (193 nm, New Wave Research Inc., Shanghai, China). The laser spot size was set to 32 μm for most of the analyses, with a laser energy density of 10 J/cm^2 and a repetition rate of 8 Hz. The laser sampling procedure consisted of a 30 s blank, followed by a 30 s sampling ablation, and a 2 min sample-chamber flushing after the ablation. The ablated material was carried into the ICP-MS by a high-purity Helium gas stream with a flux of 1.15 L/min. The entire laser path was fluxed with Ar (600 mL/min) to ensure energy stability. The counting times were 20 ms for ^{204}Pb, ^{206}Pb, ^{207}Pb, and ^{208}Pb, 15 ms for ^{232}Th and ^{238}U, 20 ms for ^{49}Ti, and 6 ms for other elements. NIST 610 glass was used as an external standard and Si as an internal standard for calibrations in the zircon analyses. U-Pb isotope fractionation effects were corrected using zircon 91500 [43] as an external standard. Isotopic ratios and element concentrations of zircons were calculated using Glitter [44]. Concordia ages and diagrams were obtained using Isoplot/Ex (3.0) [44]. The common lead was corrected using LA-ICP-MS Common Lead Correction (ver. 3.15), following the method of Andersen (2002) [45]. The analytical data are presented on U-Pb Concordia diagrams with 1σ errors. The mean ages are weighted means at 95% confidence levels [44]. The analyses of four samples were conducted at the Key laboratory of Mineral Resources Evaluation in Northeast Asia, Ministry of Natural Resources. The data are listed in Table 2.

Table 2. LA-ICP-MS zircon U-Pb dating data of mafic rocks from northern Liaoning.

Sample No.	Pb	Th	U	Th/U	Isotopic Ratios						Ages (Ma)					
					^{207}Pb/^{206}Pb		^{207}Pb/^{235}U		^{206}Pb/^{238}U		^{207}Pb/^{206}Pb		^{207}Pb/^{235}U		^{206}Pb/^{238}U	
	μg/g	μg/g	μg/g		Ratio	1σ	Ratio	1σ	Ratio	1σ	Ages	1σ	Ages	1σ	Ages	1σ
D1917-1	147	204	204	1.00	0.16593	0.00205	11.11433	0.14256	0.48580	0.00550	2517	10	2533	12	2552	24
D1917-2	113	152	158	0.97	0.16924	0.00222	11.30379	0.15295	0.48440	0.00559	2550	10	2549	13	2546	24
D1917-3	165	151	248	0.61	0.16773	0.00201	11.23557	0.14037	0.48583	0.00546	2535	9	2543	12	2553	24
D1917-4	80	96	115	0.84	0.15909	0.00245	10.67661	0.16715	0.48672	0.00591	2446	12	2495	15	2556	26
D1917-5	104	126	150	0.84	0.16642	0.00228	11.13507	0.15676	0.48528	0.00568	2522	11	2534	13	2550	25
D1917-6	136	173	256	0.67	0.13358	0.00185	7.24344	0.10270	0.39328	0.00453	2146	11	2142	13	2138	21
D1917-7	248	208	383	0.54	0.15805	0.00210	10.60423	0.14510	0.48660	0.00562	2435	10	2489	13	2556	24
D1917-8	55	166	181	0.92	0.16471	0.00251	11.02476	0.17113	0.48546	0.00590	2505	12	2525	14	2551	26
D1917-9	107	142	175	0.81	0.17198	0.00301	11.50736	0.20313	0.48529	0.00629	2577	14	2565	16	2550	27
D1917-10	34	53	48	1.11	0.16709	0.00336	11.17697	0.22481	0.48516	0.00669	2529	17	2538	19	2550	29
D1917-11	181	241	263	0.92	0.16475	0.00252	11.02789	0.17202	0.48548	0.00593	2505	12	2525	15	2551	26
D1917-12	110	16	190	0.08	0.11216	0.00165	5.06862	0.07596	0.32775	0.00379	1835	13	1831	13	1827	18
D1917-13	56	63	84	0.75	0.16491	0.00264	11.03467	0.17975	0.48530	0.00604	2507	13	2526	15	2550	26
D1917-14	126	108	198	0.54	0.17321	0.00275	11.59110	0.18697	0.48534	0.00605	2589	13	2572	15	2550	26
D1917-15	81	85	132	0.64	0.16791	0.00233	11.23826	0.16055	0.48543	0.00575	2537	11	2543	13	2551	25
D1917-16	86	100	168	0.60	0.13479	0.00178	7.34147	0.10054	0.39503	0.00453	2161	11	2154	12	2146	21
D1917-17	40	52	67	0.78	0.16737	0.00265	11.20165	0.18090	0.48541	0.00604	2532	13	2540	15	2551	26
D1917-18	156	204	233	0.87	0.16325	0.00198	10.92303	0.13888	0.48530	0.00553	2490	10	2517	12	2550	24
D1918-1	433	579	329	1.76	0.12674	0.00165	4.73294	0.06320	0.27084	0.00302	2053	11	1773	11	1545	15
D1918-2	66	192	346	0.55	0.06855	0.00126	1.27825	0.02361	0.10524	0.00155	885	20	836	11	618	9
D1918-3	34	199	325	0.61	0.06050	0.00145	0.56447	0.01342	0.06766	0.00081	622	31	454	9	422	5
D1918-4	11	47	23	2.07	0.13647	0.00693	5.34881	0.26801	0.28956	0.00662	2183	54	1853	42	1639	33
D1918-5	105	156	295	0.53	0.13855	0.00200	7.80004	0.11473	0.40831	0.00472	2209	12	2208	13	2207	22
D1918-6	19	353	401	0.88	0.05312	0.00189	0.29153	0.01019	0.05181	0.00053	334	55	260	8	352	3
D1919-1	551	998	1166	0.86	0.12831	0.00145	6.72157	0.07992	0.37990	0.00419	2075	9	2075	11	2076	20
D1919-2	372	565	819	0.69	0.11940	0.00128	4.47229	0.05086	0.27164	0.00296	1947	9	1726	9	1549	15
D1919-3	328	1128	1005	1.12	0.11497	0.00187	3.19372	0.05222	0.20145	0.00237	1879	14	1456	13	1183	13
D1919-4	187	322	396	0.81	0.12081	0.00168	5.02826	0.07156	0.30184	0.00345	1968	12	1824	12	1700	17
D1919-5	432	597	962	0.62	0.11532	0.00150	4.79112	0.06421	0.30130	0.00338	1885	11	1783	11	1698	17
D1919-6	714	1159	871	1.33	0.12667	0.00198	6.55743	0.10378	0.37542	0.00445	2052	13	2054	14	2055	21
D1919-7	799	1533	843	1.82	0.11443	0.00129	3.09836	0.03670	0.19636	0.00214	1871	10	1432	9	1156	12
D1919-8	694	1404	1140	1.23	0.11692	0.00131	3.17513	0.03728	0.19694	0.00214	1910	9	1451	9	1159	12
D1919-9	806	181	254	0.71	0.12653	0.00137	5.71060	0.06523	0.32730	0.00355	2050	9	1933	10	1825	17
D1919-10	611	1042	1350	0.77	0.12085	0.00134	4.63869	0.05410	0.27837	0.00303	1969	9	1756	10	1583	15
D1919-11	537	698	1196	0.58	0.12378	0.00151	5.18714	0.06559	0.30390	0.00336	2011	10	1851	11	1711	17
D1919-12	399	435	930	0.47	0.11951	0.00171	4.96315	0.07215	0.30119	0.00343	1949	12	1813	12	1697	17
D1919-13	578	767	1327	0.58	0.12760	0.00138	6.64670	0.07600	0.37777	0.00409	2065	9	2066	10	2066	19
D1919-14	597	1330	1279	1.04	0.11898	0.00138	4.61516	0.05564	0.28131	0.00307	1941	10	1752	10	1598	15
D1919-15	628	1179	1345	0.88	0.12776	0.00147	6.66303	0.08020	0.37825	0.00413	2067	9	2068	11	2068	19

Table 2. *Cont.*

Sample No.	Pb	Th	U	Th/U	Isotopic Ratios						Ages (Ma)					
	μg/g	μg/g	μg/g		$^{207}Pb/^{206}Pb$		$^{207}Pb/^{235}U$		$^{206}Pb/^{238}U$		$^{207}Pb/^{206}Pb$		$^{207}Pb/^{235}U$		$^{206}Pb/^{238}U$	
					Ratio	1σ	Ratio	1σ	Ratio	1σ	Ages	1σ	Ages	1σ	Ages	1σ
D1919-16	758	1279	867	1.48	0.12795	0.00148	6.64009	0.08005	0.37640	0.00411	2070	9	2065	11	2059	19
D1919-17	247	373	539	0.69	0.12699	0.00204	6.45484	0.10483	0.36867	0.00437	2057	14	2040	14	2023	21
D1919-18	268	222	426	0.52	0.12721	0.00198	6.48693	0.10213	0.36985	0.00433	2060	13	2044	14	2029	20
D1919-19	610	836	1352	0.62	0.11767	0.00132	4.44471	0.05225	0.27399	0.00296	1921	9	1721	10	1561	15
D1919-20	763	921	791	1.16	0.12337	0.00164	4.68489	0.06379	0.27543	0.00307	2006	11	1765	11	1568	16
D2012-1	223	612	385	1.59	0.12430	0.00309	6.28771	0.16997	0.36747	0.00890	2019	21	2017	24	2017	42
D2012-2	78	97	102	0.95	0.15723	0.00568	9.88062	0.36881	0.45644	0.01234	2426	30	2424	34	2424	55
D2012-3	79	104	89	1.17	0.12421	0.01113	7.42792	0.65583	0.43433	0.01872	2018	36	2164	79	2325	84
D2012-4	53	141	144	0.98	0.12424	0.01331	4.55272	0.46856	0.26612	0.01318	2018	23	1741	86	1521	67
D2012-5	322	647	422	1.53	0.12418	0.00274	5.65294	0.13968	0.33053	0.00789	2017	20	1924	21	1841	38
D2012-6	83	117	178	0.66	0.12429	0.00296	6.17418	0.16200	0.36066	0.00872	2019	21	2001	23	1985	41
D2012-7	338	376	628	0.60	0.15747	0.00470	9.93961	0.31371	0.45823	0.01188	2429	24	2429	29	2432	53
D2012-8	98	151	155	0.98	0.15584	0.00733	9.78661	0.46316	0.45576	0.01418	2411	41	2415	44	2421	63
D2012-9	262	786	490	1.60	0.12434	0.00329	6.02196	0.17227	0.35136	0.00873	2019	23	1979	25	1941	42
D2012-10	490	1059	936	1.13	0.12424	0.00285	4.68979	0.12025	0.27383	0.00664	2018	20	1765	21	1560	34
D2012-11	301	263	553	0.48	0.15727	0.00436	9.87122	0.29528	0.45526	0.01168	2427	23	2423	28	2419	52
D2012-12	169	155	319	0.48	0.15791	0.00332	9.89645	0.23891	0.45448	0.01100	2433	19	2425	22	2415	49
D2012-13	586	999	675	1.48	0.12436	0.00279	5.90907	0.14947	0.34455	0.00839	2020	20	1963	22	1909	40
D2012-14	87	136	211	0.64	0.12432	0.01120	5.79273	0.51744	0.33781	0.01512	2019	16	1945	77	1876	73
D2012-15	313	1264	735	1.72	0.12418	0.00345	6.76699	0.20284	0.39505	0.01003	2017	24	2081	27	2146	46
D2012-16	166	178	302	0.59	0.15738	0.00401	9.93189	0.27757	0.45748	0.01156	2428	21	2428	26	2428	51
D2012-17	87	89	111	0.80	0.15522	0.01408	9.77099	0.86913	0.45628	0.02187	2404	38	2413	82	2423	97

3.3. Major and Trace Element Analyses

After conducting major, trace, and rare earth element (REE) analyses for 28 samples, the results were obtained from the Northeast China Supervision and Inspection Center of Mineral Resources, Ministry of Natural Resources (Shenyang, China). The samples underwent petrographic examination and the altered rock surfaces were removed before being crushed and ground to 74 μm using an agate mill. The major element contents of the whole rock were determined using X-ray fluorescence spectrometry (XRF), with analytical precisions exceeding 2%. The trace element and REE contents were determined using X Series II ICP-MS from American Thermal Power Company in Salt Lake City Utah State. A total of 0.1 g of the sample was placed in a digestion tank, with 1 mL of concentrated nitric acid and 1 mL of hydrofluoric acid added. The digestion tank was placed in an oven and was heated up to 180 degrees for 10–12 h. After removal, it was heated at 120 degrees on an electric heating plate in an open environment. When about 2–3 mL of the digestion solution was left, it was heated up to 240 degrees. After redissolving, 0.5% dilute nitric acid was added to the mark for measurement. Twelve measurements were conducted on samples, with analytical precisions exceeding 5% for elements with contents of >10 μg/g, exceeding 8% for elements with contents of <10 μg/g, and 10% for the transition metals. The results are listed in Table 3.

Table 3. Major element (%), rare element, and trace element (μg/g) composition of mafic rocks from northern Liaoning.

Sample No.	D1918-1	D1918-2	D1918-3	D1918-4	D1918-5	D1918-6	D1917-1	D1917-2	D1917-3	D1917-4	D1917-5	D1917-6	D1917-7	D1917-8
Lithology	**Diabase**						**Basalt**							
SiO_2	51.11	52.86	50.22	50.13	49.04	48.60	47.51	49.81	48.59	50.38	49.71	50.42	47.03	51.18
TiO_2	1.60	1.63	1.59	1.61	1.65	1.61	2.35	2.36	2.51	2.49	2.36	2.36	2.37	2.33
Al_2O_3	13.34	12.95	13.41	13.13	13.14	13.33	14.36	14.08	14.90	14.41	14.13	13.86	14.20	13.56
Fe_2O_3	1.85	1.39	2.96	3.22	3.31	3.69	3.72	2.18	2.86	2.38	2.54	1.79	2.84	0.40
FeO	11.82	11.40	11.54	11.24	12.06	11.60	12.08	11.99	12.18	11.39	11.77	11.90	12.28	12.13
MnO	0.19	0.19	0.22	0.22	0.24	0.22	0.22	0.20	0.20	0.18	0.20	0.20	0.21	0.18
MgO	6.30	6.23	6.28	6.52	6.73	6.91	6.80	6.80	6.67	7.05	6.87	6.90	6.30	6.76
CaO	9.55	9.18	9.34	9.61	9.48	9.98	6.69	6.23	6.02	5.40	6.41	6.55	8.79	7.59
Na_2O	2.01	1.97	2.18	1.96	2.08	1.91	4.24	4.45	4.31	4.29	4.42	4.40	3.38	3.60
K_2O	0.80	1.04	0.99	1.12	0.76	0.92	0.39	0.34	0.37	0.33	0.33	0.31	0.60	0.44
P_2O_5	0.18	0.17	0.18	0.18	0.20	0.20	0.27	0.25	0.27	0.24	0.25	0.24	0.26	0.22
LOI	1.23	1.01	1.11	1.05	1.30	1.08	1.34	1.24	1.15	1.44	1.11	1.15	1.72	1.65
SUM	99.97	100.01	100.01	99.99	99.98	100.03	99.96	99.93	100.03	99.98	100.09	100.07	99.97	100.04
$Mg^{\#}$	45.69	46.99	44.32	45.35	44.63	45.45	44.25	46.74	44.86	48.41	46.78	47.91	43.33	49.36
A/NK	3.2	2.97	2.88	2.95	3.1	3.23	1.94	1.83	1.99	1.95	1.85	1.83	2.29	2.12
A/CNK	0.74	0.71	0.72	0.69	0.73	0.69	0.91	0.9	0.99	1.08	0.88	0.85	0.81	0.86
R1	2412	2503	2226	2257	2227	2212	1417	1544	1483	1635	1540	1616	1663	1959
R2	1593	1545	1574	1609	1606	1671	1336	1282	1266	1211	1302	1314	1532	1413
La	13.1	13.1	13.4	12.2	12.3	12.5	19.0	18.2	20.3	20.0	18.9	20.3	19.5	18.81
Ce	26.9	26.6	27.1	25.3	27.3	25.4	39.8	41.1	42.9	41.1	39.9	42.5	40.7	40.45
Pr	3.8	3.7	3.80	3.69	3.6	3.57	5.96	5.66	6.44	6.17	5.85	6.19	6.04	6.01
Nd	17.3	16.7	17.2	16.6	16.2	16.4	26.4	25.4	28.5	27.8	25.8	27.8	27.1	27.2
Sm	4.56	4.30	4.42	4.34	4.17	4.20	6.04	5.91	6.50	6.44	5.94	6.38	6.28	6.30
Eu	1.57	1.44	1.42	1.40	1.35	1.39	1.56	1.41	1.53	1.43	1.56	1.69	1.71	1.72
Gd	4.69	4.62	4.64	4.56	4.37	4.56	5.54	5.29	5.88	5.66	5.32	5.72	5.70	5.68
Tb	1.01	0.97	0.98	0.97	0.92	0.93	1.04	0.98	1.05	1.03	1.02	1.06	1.04	1.02
Dy	6.10	6.01	6.07	6.05	5.83	5.87	5.76	5.41	5.81	5.58	5.54	5.76	5.66	5.62
Ho	1.26	1.21	1.24	1.24	1.20	1.19	1.04	1.02	1.07	1.01	1.04	1.06	1.06	1.06
Er	3.51	3.45	3.63	3.54	3.35	3.36	2.72	2.64	2.73	2.69	2.81	2.80	2.71	2.74
Tm	0.55	0.54	0.54	0.55	0.51	0.53	0.40	0.39	0.42	0.40	0.42	0.41	0.41	0.41
Yb	3.71	3.60	3.71	3.61	3.42	3.51	2.45	2.50	2.62	2.55	2.62	2.54	2.57	2.56
Lu	0.55	0.53	0.54	0.54	0.52	0.52	0.35	0.35	0.37	0.37	0.37	0.38	0.37	0.38
ΣREE	88.6	86.9	88.6	84.6	85.0	84.0	118.1	116.2	126.1	122.2	117.1	124.5	120.8	119.9
LREE	67.3	66.0	67.3	63.6	64.9	63.5	98.8	97.6	106.1	102.9	97.9	104.8	101.3	100.5
HREE	21.4	20.9	21.3	21.0	20.1	20.5	19.3	18.6	20.0	19.3	19.1	19.7	19.5	19.5
LREE/HREE	3.15	3.15	3.15	3.02	3.23	3.10	5.12	5.26	5.32	5.34	5.12	5.31	5.19	5.16
La_N/Yb_N	2.54	2.62	2.60	2.43	2.58	2.56	5.55	5.22	5.56	5.63	5.17	5.72	5.43	5.26
Eu/Eu*	1.04	0.99	0.96	0.96	0.96	0.97	0.82	0.77	0.76	0.72	0.85	0.86	0.87	0.88
Ce/Ce*	0.93	0.93	0.93	0.92	1.01	0.93	0.92	0.99	0.92	0.91	0.93	0.93	0.92	0.93

Table 3. *Cont.*

Sample No.	D1918-1	D1918-2	D1918-3	D1918-4	D1918-5	D1918-6	D1917-1	D1917-2	D1917-3	D1917-4	D1917-5	D1917-6	D1917-7	D1917-8
Lithology	**Diabase**						**Basalt**							
Y	26.9	27.6	26.7	27.6	26.3	26.7	24.7	23.6	24.6	24.4	25.0	25.5	25.2	25.02
Sc	43	43	42	44	44	44	32	33	34	34	33	33	33	33
V	311	317	307	308	324	330	338	349	376	373	353	356	349	348
Cr	108	111	94	103	116	106	112	117	125	130	123	126	124	123
Co	49.8	49.9	50.5	51.7	52.2	53.1	42.3	41.3	41.5	42.3	51.2	50.7	51.6	49.1
Ni	71.3	73.6	71.9	75.5	75.1	74.2	75.1	67.7	72.0	75.1	68.9	70.1	71.9	73.0
Be	0.8	0.8	0.8	0.8	0.8	0.9	1.6	1.5	1.4	1.5	1.6	1.5	1.0	1.11
Rb	20	30	21	31	14	23	4	5	5	4	4	4	7	6
Sr	188	165	162	164	160	176	210	209	272	273	215	232	284	263
Ba	152	218	276	250	193	138	144	128	185	200	140	151	334	286
Zr	109	104	106	102	106	106	144	149	154	162	150	162	151	148
Nb	13.5	13.0	13.7	13.3	12.2	12.0	20.3	21.1	21.7	21.5	19.8	21.7	21.8	21.3
Hf	3.58	3.43	3.60	3.44	3.50	3.50	4.50	4.69	4.84	5.06	4.91	4.99	4.70	4.65
Ta	0.82	0.79	0.82	0.84	0.86	0.85	1.23	1.30	1.35	1.41	1.30	1.24	1.21	1.21
Th	1.86	1.67	1.73	1.53	1.68	3.62	1.31	1.36	1.73	1.71	1.35	3.47	1.86	1.67
U	0.4	0.4	0.4	0.4	0.4	0.4	0.4	0.3	0.4	0.4	0.3	0.8	0.6	0.39
$(La/Sm)_N$	1.86	1.97	1.96	1.81	1.90	1.93	2.03	1.99	2.01	2.01	2.05	2.05	2.00	1.93
La/Sm	2.88	3.05	3.04	2.81	2.94	2.98	3.14	3.08	3.12	3.11	3.18	3.17	3.10	2.99
Ta/Yb	0.22	0.22	0.22	0.23	0.25	0.24	0.50	0.52	0.51	0.55	0.50	0.49	0.47	0.47
Th/Yb	0.50	0.46	0.47	0.42	0.49	1.03	0.53	0.54	0.66	0.67	0.52	1.37	0.72	0.65
Ce/Yb	7.26	7.40	7.30	7.02	8.00	7.22	16.2	16.4	16.4	16.1	15.2	16.8	15.9	15.8
La/Yb	3.54	3.65	3.62	3.38	3.60	3.57	7.74	7.28	7.74	7.84	7.21	7.98	7.57	7.34
Sc/Ni	0.60	0.58	0.59	0.58	0.59	0.59	0.42	0.48	0.48	0.46	0.48	0.47	0.46	0.45
Zr/Y	4.04	3.77	3.99	3.70	4.05	3.96	5.84	6.33	6.28	6.66	5.99	6.38	6.00	5.91
Nb/Y	0.50	0.47	0.51	0.48	0.46	0.45	0.82	0.89	0.88	0.88	0.79	0.85	0.87	0.85
Nb/Th	7.24	7.79	7.90	8.71	7.29	3.33	15.5	15.5	12.6	12.5	14.6	6.2	11.8	12.8
La/Nb	0.98	1.01	0.98	0.92	1.01	1.04	0.94	0.86	0.93	0.93	0.95	0.93	0.89	0.88
Ba/Nb	11.30	16.72	20.16	18.81	15.76	11.48	7.12	6.07	8.52	9.30	7.06	6.96	15.3	13.4
Th/Yb	0.50	0.46	0.47	0.42	0.49	1.03	0.53	0.54	0.66	0.67	0.52	1.37	0.72	0.65
Zr/Nb	8.06	7.99	7.78	7.68	8.71	8.78	7.11	7.08	7.11	7.56	7.56	7.50	6.91	6.94
Th/Zr	0.02	0.02	0.02	0.01	0.02	0.03	0.01	0.01	0.01	0.01	0.01	0.02	0.01	0.01
Ba/La	11.59	16.57	20.53	20.54	15.68	11.02	7.61	7.04	9.12	9.97	7.41	7.45	17.2	15.2
La/Yb	3.54	3.65	3.62	3.38	3.60	3.57	7.74	7.28	7.74	7.84	7.21	7.98	7.57	7.34
Zr/Hf	30.36	30.25	29.55	29.69	30.39	30.20	32.05	31.86	31.82	32.06	30.55	32.58	32.11	31.83
Hf/Ta	4.34	4.34	4.40	4.11	4.06	4.13	3.65	3.61	3.60	3.59	3.77	4.02	3.87	3.84
La/Ta	15.95	16.59	16.43	14.56	14.24	14.79	15.41	14.01	15.06	14.21	14.51	16.33	16.02	15.52
Th/Ta	2.26	2.11	2.12	1.83	1.94	4.27	1.06	1.05	1.28	1.21	1.04	2.80	1.53	1.38
Ta/Hf	0.23	0.23	0.23	0.24	0.25	0.24	0.27	0.28	0.28	0.28	0.27	0.25	0.26	0.26
Th/Hf	0.52	0.49	0.48	0.44	0.48	1.03	0.29	0.29	0.36	0.34	0.28	0.70	0.40	0.36

Table 3. *Cont.*

Sample No.	D1917-9	D1917-10	D1919-1	D1919-2	D1919-3	D1919-4	D1919-5	D1919-6	D2012-1	D2012-2	D2012-3	D2012-4	D2012-5	D2012-6
Lithology	**Basalt**				**Gabbro**						**Amphibolite**			
SiO_2	47.72	50.34	48.83	51.17	47.03	51.02	48.93	51.44	45.29	46.10	48.37	46.63	45.46	46.48
TiO_2	2.36	2.38	2.15	2.16	2.21	2.14	2.19	2.14	1.90	2.00	1.73	1.99	2.29	1.70
Al_2O_3	14.33	13.97	15.03	14.55	15.10	14.70	14.98	14.83	14.46	14.82	14.26	14.07	14.05	15.00
Fe_2O_3	2.99	1.71	3.61	2.39	5.67	2.36	4.11	2.87	2.36	2.53	1.88	1.14	2.34	2.52
FeO	11.76	11.52	9.24	9.65	9.15	9.86	9.35	9.20	11.35	11.94	11.57	13.10	13.29	9.24
MnO	0.20	0.18	0.19	0.19	0.17	0.16	0.15	0.15	0.19	0.24	0.21	0.21	0.22	0.16
MgO	6.54	6.30	6.18	6.38	6.31	6.17	6.12	5.87	7.17	7.65	7.11	8.51	7.85	6.72
CaO	7.80	7.55	7.35	7.12	7.45	7.02	7.34	6.75	11.45	9.32	8.35	8.74	8.19	13.98
Na_2O	3.40	3.77	3.30	3.38	3.22	3.33	3.44	3.45	2.05	3.02	3.29	2.62	3.07	1.61
K_2O	0.64	0.48	1.68	1.57	1.89	1.78	1.68	1.80	1.78	1.14	1.60	1.09	1.17	1.15
P_2O_5	0.26	0.24	0.39	0.36	0.43	0.38	0.41	0.38	0.19	0.20	0.17	0.19	0.22	0.16
LOI	1.97	1.59	2.02	1.02	1.36	1.11	1.22	1.05	1.76	1.08	1.40	1.71	1.81	1.34
SUM	99.99	100.05	99.96	99.94	99.99	100.04	99.93	99.94	99.93	100.03	99.94	100.01	99.97	100.05
$Mg^{\#}$	44.87	46.47	47.11	49.33	44.34	48.10	45.78	47.26	48.91	49.22	49.11	52.03	47.84	51.23
A/NK	2.28	2.08	2.08	2.00	2.06	1.98	2.01	1.94	2.73	2.39	2.00	2.56	2.22	3.85
A/CNK	0.94	0.86	1.00	0.86	0.90	0.88	0.88	0.90	0.67	0.74	0.76	0.83	0.85	0.58
R1	1687	1796	1546	1727	1371	1684	1488	1655	1765	1617	1591	1840	1547	2148
R2	1441	1394	1389	1364	1407	1345	1384	1305	1865	1667	1527	1633	1542	2122
La	19.87	20.17	22.94	19.91	22.20	21.69	21.20	23.28	12.58	12.56	11.95	13.95	13.42	11.02
Ce	41.42	42.64	43.30	38.81	43.12	41.29	41.12	43.74	28.70	28.83	26.09	32.84	30.75	23.93
Pr	6.19	6.35	6.06	5.45	6.05	5.78	5.70	6.19	4.22	4.45	3.84	4.57	4.39	3.50
Nd	27.55	28.67	26.64	24.08	26.32	25.13	24.91	27.15	17.63	19.56	15.88	19.33	19.15	15.07
Sm	6.32	6.54	5.57	5.15	5.77	5.27	5.23	5.61	4.59	4.94	4.30	4.73	5.30	3.70
Eu	1.72	1.64	2.31	2.11	2.38	2.15	2.24	2.28	1.50	1.60	1.42	1.72	1.64	1.42
Gd	5.84	5.88	5.13	4.71	5.04	4.82	4.75	5.08	3.86	4.73	4.25	4.56	4.78	3.98
Tb	1.06	1.09	0.88	0.82	0.91	0.84	0.84	0.89	0.60	0.76	0.66	0.78	0.90	0.55
Dy	5.74	5.87	4.62	4.40	4.82	4.55	4.34	4.64	3.82	4.08	3.38	4.00	4.89	3.64
Ho	1.06	1.10	0.88	0.86	0.90	0.86	0.82	0.89	0.73	0.71	0.70	0.75	0.75	0.74
Er	2.72	2.90	2.28	2.23	2.34	2.27	2.15	2.28	1.88	2.13	1.75	2.17	2.48	1.94
Tm	0.41	0.42	0.35	0.33	0.34	0.34	0.33	0.34	0.32	0.30	0.25	0.32	0.36	0.26
Yb	2.60	2.69	2.24	2.09	2.19	2.15	2.01	2.19	1.95	2.19	1.64	1.81	2.03	1.79
Lu	0.37	0.38	0.31	0.30	0.32	0.31	0.29	0.31	0.23	0.31	0.28	0.30	0.33	0.24
ΣREE	122.9	126.3	123.5	111.3	122.7	117.4	115.9	124.9	82.6	87.1	76.4	91.8	91.2	71.8
LREE	103.1	106.0	106.8	95.5	105.8	101.3	100.4	108.2	69.2	71.9	63.5	77.1	74.7	58.6
HREE	19.8	20.3	16.7	15.8	16.9	16.1	15.5	16.6	13.4	15.2	12.9	14.7	16.5	13.1
LREE/HREE	5.21	5.21	6.40	6.06	6.28	6.28	6.46	6.51	5.17	4.73	4.92	5.25	4.52	4.47
La_N/Yb_N	5.48	5.39	7.36	6.82	7.28	7.25	7.55	7.63	4.64	4.12	5.24	5.52	4.74	4.42
Eu/Eu*	0.87	0.81	1.32	1.31	1.35	1.30	1.37	1.31	1.09	1.01	1.01	1.13	0.99	1.13
Ce/Ce*	0.92	0.92	0.90	0.91	0.91	0.90	0.92	0.89	0.97	0.94	0.94	1.01	0.98	0.95

Table 3. *Cont.*

Sample No.	D1917-9	D1917-10	D1919-1	D1919-2	D1919-3	D1919-4	D1919-5	D1919-6	D2012-1	D2012-2	D2012-3	D2012-4	D2012-5	D2012-6
Lithology	**Basalt**				**Gabbro**						**Amphibolite**			
Y	25.78	26.19	22.19	20.70	22.47	21.39	21.24	22.17	18.01	19.70	17.93	19.16	22.90	17.96
Sc	32	32	27	27	27	27	27	27	24	25	25	26	30	22
V	346	337	293	297	310	303	299	294	250	264	248	267	306	228
Cr	122	127	99	99	107	167	105	101	140	123	137	127	125	126
Co	51.3	46.4	68.5	60.0	61.6	56.7	66.9	62.7	50.3	45.8	46.8	50.7	53.2	43.8
Ni	70.8	69.4	82.3	75.2	66.7	72.4	69.7	77.6	105.3	96.6	97.1	107.7	91.5	91.8
Be	1.09	1.09	0.95	0.98	0.94	1.03	0.94	0.97	1.07	1.19	1.23	1.20	1.13	1.58
Rb	8.36	6.16	38.05	35.93	40.14	40.37	38.06	42.54	41.35	30.96	51.02	33.16	28.29	27.77
Sr	251	235	439	429	372	406	412	423	154	327	413	272	370	138
Ba	362	344	715	737	682	839	650	733	59	179	99	175	115	47
Zr	157	158	117	101	111	111	100	117	112	116	102	124	135	106
Nb	21.1	20.2	9.0	9.0	9.2	8.6	10.7	10.2	11.3	11.4	10.0	11.1	13.1	10.2
Hf	4.83	5.00	3.65	3.36	3.61	3.57	3.11	3.64	3.25	3.73	3.13	3.83	3.89	2.96
Ta	1.25	1.26	0.63	0.62	0.60	0.61	0.64	0.67	0.87	0.97	0.63	0.96	0.67	0.44
Th	1.68	1.88	2.45	2.04	2.13	1.65	1.67	2.05	0.94	1.16	0.89	1.19	0.94	0.76
U	0.36	0.33	0.37	0.42	0.42	0.29	0.32	0.34	0.25	0.25	0.16	0.23	0.24	0.16
$(La/Sm)_N$	2.03	1.99	2.66	2.50	2.48	2.66	2.62	2.68	1.77	1.64	1.80	1.90	1.63	1.92
La/Sm	3.14	3.08	4.12	3.87	3.85	4.12	4.06	4.15	2.74	2.54	2.78	2.95	2.53	2.98
Ta/Yb	0.48	0.47	0.28	0.29	0.27	0.28	0.32	0.30	0.45	0.45	0.39	0.53	0.33	0.25
Th/Yb	0.65	0.70	1.10	0.97	0.97	0.77	0.83	0.94	0.48	0.53	0.54	0.66	0.46	0.43
Ce/Yb	15.9	15.9	19.4	18.5	19.7	19.2	20.4	20.0	14.7	13.2	16.0	18.1	15.1	13.4
La/Yb	7.64	7.51	10.26	9.51	10.15	10.11	10.53	10.64	6.46	5.74	7.31	7.70	6.61	6.16
Sc/Ni	0.46	0.46	0.33	0.36	0.41	0.37	0.39	0.34	0.23	0.26	0.25	0.24	0.33	0.24
Zr/Y	6.07	6.02	5.26	4.90	4.95	5.20	4.72	5.26	6.23	5.91	5.68	6.49	5.90	5.89
Nb/Y	0.82	0.77	0.40	0.43	0.41	0.40	0.50	0.46	0.63	0.58	0.56	0.58	0.57	0.57
Nb/Th	12.55	10.74	3.66	4.40	4.30	5.22	6.41	4.96	12.03	9.86	11.27	9.35	13.97	13.37
La/Nb	0.94	1.00	2.56	2.22	2.43	2.52	1.98	2.28	1.12	1.10	1.20	1.25	1.03	1.08
Ba/Nb	17.1	17.0	79.8	82.3	74.5	97.6	60.8	71.9	5.2	15.7	10.0	15.7	8.8	4.6
Th/Yb	0.65	0.70	1.10	0.97	0.97	0.77	0.83	0.94	0.48	0.53	0.54	0.66	0.46	0.43
Zr/Nb	7.42	7.80	13.01	11.31	12.16	12.93	9.39	11.45	9.96	10.21	10.20	11.17	10.34	10.35
Th/Zr	0.01	0.01	0.02	0.02	0.02	0.01	0.02	0.02	0.01	0.01	0.01	0.01	0.01	0.01
Ba/La	18.2	17.1	31.2	37.0	30.7	38.7	30.7	31.5	4.7	14.2	8.33	12.54	8.56	4.26
La/Yb	7.64	7.51	10.26	9.51	10.15	10.11	10.53	10.64	6.46	5.74	7.31	7.70	6.61	6.16
Zr/Hf	32.42	31.54	31.94	30.12	30.83	31.17	32.23	32.09	34.54	31.26	32.57	32.44	34.72	35.68
Hf/Ta	3.87	3.97	5.80	5.46	6.02	5.85	4.83	5.46	3.72	3.83	4.93	3.98	5.79	6.68
La/Ta	15.92	16.02	36.47	32.33	37.02	35.60	32.90	34.92	14.43	12.90	18.85	14.49	19.97	24.84
Th/Ta	1.35	1.50	3.90	3.31	3.55	2.70	2.59	3.08	1.07	1.19	1.40	1.24	1.39	1.72
Ta/Hf	0.26	0.25	0.17	0.18	0.17	0.17	0.21	0.18	0.27	0.26	0.20	0.25	0.17	0.15
Th/Hf	0.35	0.38	0.67	0.61	0.59	0.46	0.54	0.57	0.29	0.31	0.28	0.31	0.24	0.26

4. Analytical Results

4.1. Zircon U-Pb Geochronology

Sample D1917 is a basalt collected from Xiongguantun Town Yunpangou Village in Tieling City. Eighteen isotopic analyses were conducted on 18 zircons from this sample, and can be divided into three groups. Dark edges with different widths occurred around most zircons from the first group, which may be the proliferative edges formed by recrystallization during metamorphism. They are mostly self-shaped rhombohedral with diameters of 60–140 μm and length–width ratios of 1.5:1 to 3:1, generally black, clear oscillatory zoning (Figure 4), and the combination with their higher Th/U ratios (0.54–1.11), higher contents of total rare earth elements (REEs) (average contents of 585.65 μg/g), Nb, and Ta (average contents of 1.94 μg/g and 0.58 μg/g), and a significant positive Ce anomaly and negative Eu anomaly (Figure 5a), indicates a magmatic origin [46–49]. Fifteen analyses yielded an upper intercept age of 2550 ± 16 Ma (n = 15, MSWD = 0.1), which is consistent with the $^{207}Pb/^{206}Pb$ weighted average age of 2544 ± 18 Ma (n = 9, MSWD = 3.5) (Figure 6a). The age of the first group is interpreted as the captured zircons from the surrounding Archean rocks. The second group is composed of two zircons (6, 16) with diameters of 60–70 μm and length–width ratios around 2:1 (Figure 4), which combined with their evident internal structure and Th/U ratios (0.60, 0.67), higher REEs (average contents of 840.5 μg/g), Nb, and Ta (average contents of 1.65 μg/g and 0.53 μg/g), and a significant positive Ce anomaly and negative Eu anomaly (Figure 5a), indicate a magmatic origin [46–49]. Two analyses yield a concordant weighted average $^{207}Pb/^{206}Pb$ age of 2154 ± 15 Ma (n = 2, MSWD = 0.93) (Figure 6a). Thus, this represents the magmatic crystallization age. Only one zircon (data 12) belongs to the third group. It exhibits rounded and embayed boundaries, largely homogeneous central regions with an unzoned internal structure (Figure 4) and low ratio of Th/U (0.08), lower contents of REEs (127.03 μg/g), Nb, and Ta (0.04 μg/g and 0.02 μg/g), and a flat Ce and Eu distribution (Figure 5a), which indicate a metamorphic zircon [46–49]. This zircon has a concordant $^{207}Pb/^{206}Pb$ age of 1831 ± 13 Ma (Figure 6a) and is interpreted as the time of late metamorphism.

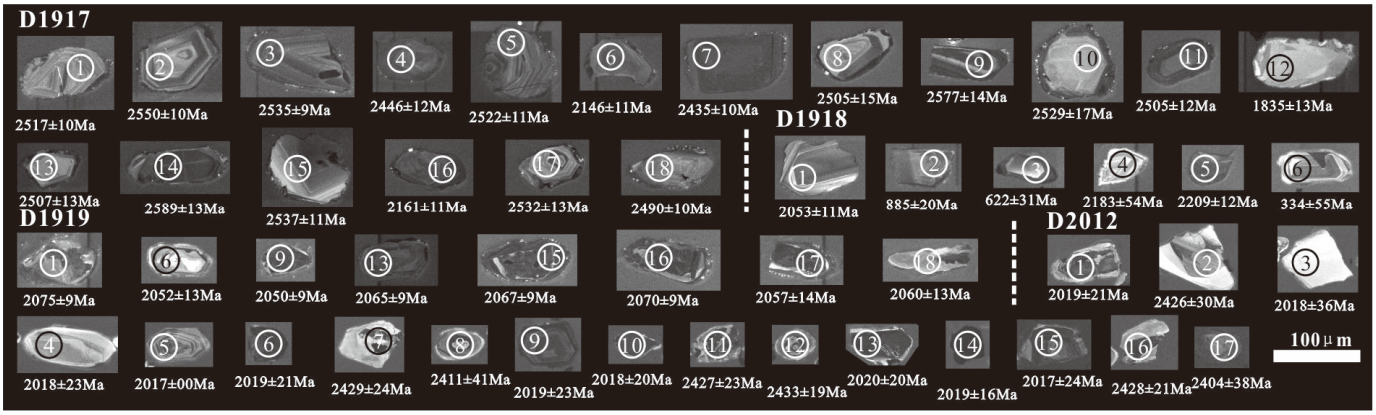

Figure 4. Cathodoluminescence (CL) images of the selected zircons from the mafic rocks in northern Liaoning. The circles on zircons represent analyzed spots.

Only six zircons have been separated from the D1918 diabase sample, and they are euhedral stubby prisms (length/width ratios 1.5:1–3:1), clear and colorless to light-brown, ranging in size from 50 to 120 μm, with larger grains being fragments presumably broken during processing. In cathodoluminescence (CL) imaging, the internal structures vary from high-CL to low-CL contrast fine oscillatory zoning in both CL-bright and CL-dark grains (Figure 4). Combined with high Th/U ratios (0.60, 0.67), higher contents of REEs (average contents of 1271.34 μg/g), Nb, and Ta (average contents of 1.96 μg/g and 0.76 μg/g), and a significant positive Ce anomaly and negative Eu anomaly (Figure 5b), this indicates that the zircons in this sample are magmatic-derived zircon [46–49]. Six analyses yielded an upper intercept age of 2203 ± 50 Ma (n = 6, MSWD = 5.7), which is consistent with the $^{207}Pb/^{206}Pb$

age (2209 ± 12 Ma) in the concordant line (Figure 6b). Thus, this age is interpreted as the time of magmatic emplacement.

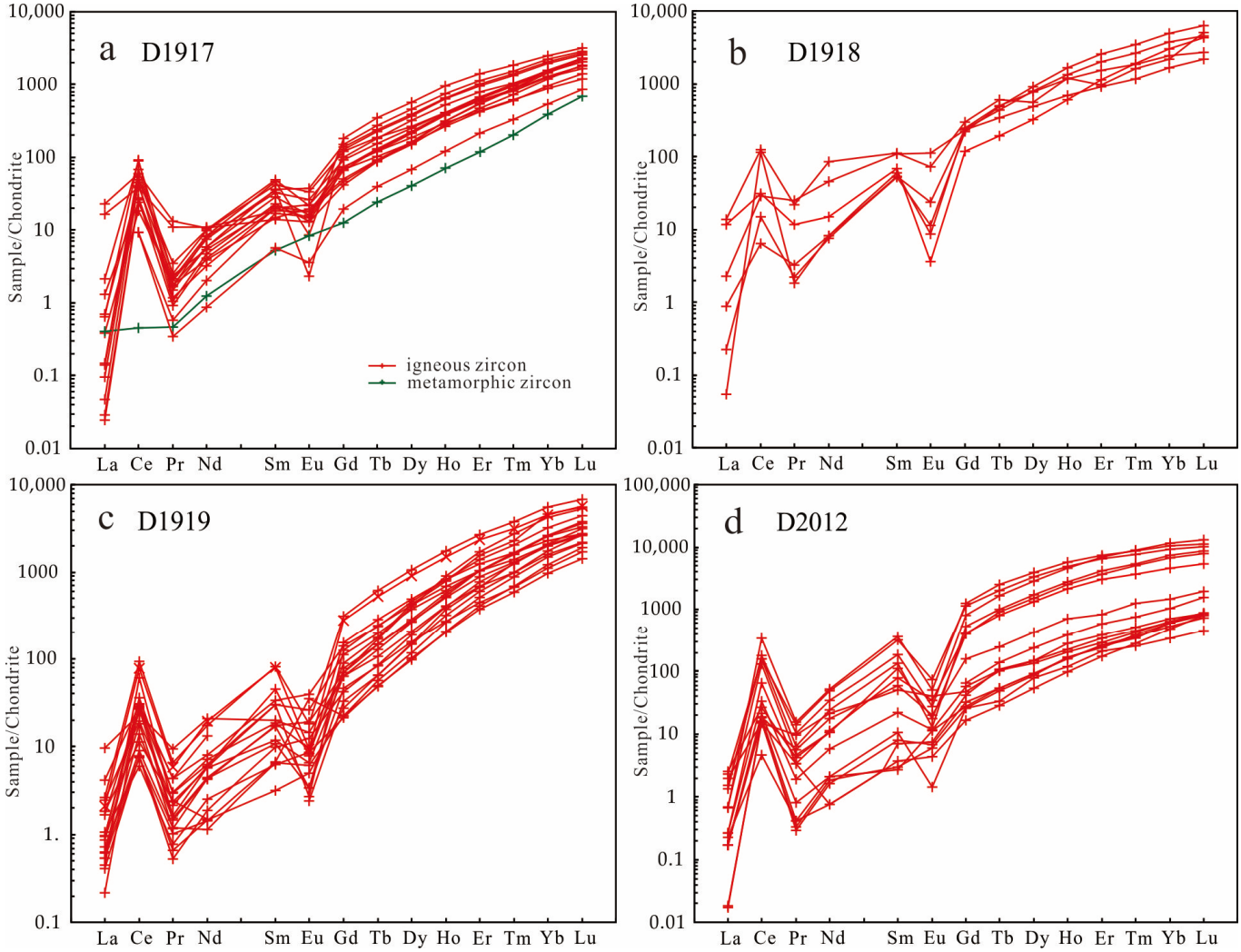

Figure 5. Chondrite-normalized REE distribution diagrams for different zircons from mafic rocks in northern Liaoning.

Zircons from the gabbro sample D1919 are euhedral prisms ranging in size from 50 to 130 μm with length/width ratios from 2:1 to 4:1 with some rounding of their apices. Although exhibiting a low contrast, CL imaging of the internal structure reveals dominantly fine oscillatory zoning (Figure 4). With the Th/U ratios ranging from 0.47 to 1.82, higher contents of REEs (average contents of 933.35 μg/g), Nb, and Ta (average contents of 2.97 μg/g and 1.19 μg/g), and a significant positive Ce anomaly and negative Eu anomaly (Figure 5c), these zircons were considered to be of magmatic origin [46–49]. A total of 20 U-Pb isotopic analyses were conducted on 20 zircons from this sample, yielding an upper intercept $^{207}Pb/^{206}Pb$ age of 2055 ± 23 Ma (n = 20, MSWD = 3.0), which is consistent with the weighted average $^{207}Pb/^{206}Pb$ age of 2063 ± 7 Ma (n = 8, MSWD = 0.18) from eight zircons on the concordant line (Figure 6c). This age is interpreted as the crystallization age of the gabbro.

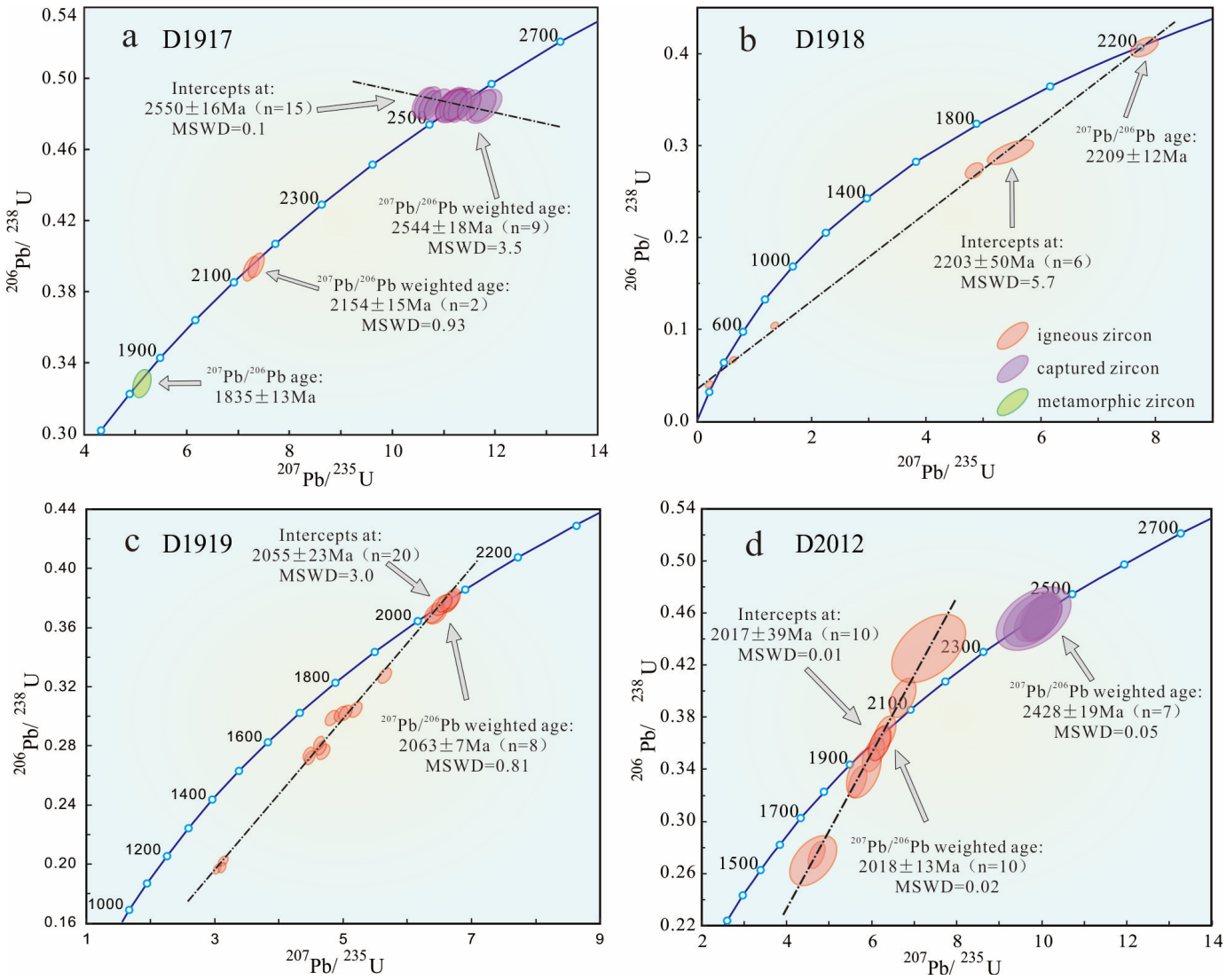

Figure 6. Concordia diagrams for zircons analysed from mafic rocks in the northern Liaoning.

Sample D2012, which was collected from Wangxiaopu Village, yielded prismatic and sub-angular zircon ranging in size from 35 μm to 120 μm with length/width ratios from 1:1 to 4:1. The zircon grains contain numerous inclusions and are divided into two groups according to the CL images (Figure 4). The rounded or irregular cores and white rims are present in these grains from the first group and are CL-dark with no obvious zoning. The ratios of Th/U range from 0.48 to 0.98, with high contents of REEs (average contents of 232.59 μg/g), Nb, and Ta (average contents of 0.95 μg/g and 0.48 μg/g), and a significant positive Ce anomaly and negative Eu anomaly (Figure 5d) indicate a magmatic origin [46–49]. Seven analyses were obtained from seven zircons, yielding a concordant $^{207}Pb/^{206}Pb$ age of 2428 ± 19 Ma (n = 7, MSWD = 0.05) (Figure 6d). Due to the small size of zircon, both the core and rim were collected during sampling, so this age represents a mixed age, and these zircons are interpreted as the captured zircons from the surrounding Archean rocks. The other groups of zircons generally have an evident internal structure with fine, oscillatory zoning and Th/U ratios (0.59–1.72), higher contents of REEs (average contents of 2736.25 μg/g), Nb and Ta (average contents of 13.40 μg/g and 1.81 μg/g), and a significant positive Ce anomaly and negative Eu anomaly (Figure 5d), which show the characteristics of magmatic origin zircon [46–49]. Ten analyses were concordant to near-concordant and yielded an upper intercept $^{207}Pb/^{206}Pb$ age of 2017 ± 39 Ma (n = 10, MSWD = 0.01), and a weighted average $^{207}Pb/^{206}Pb$ age of 2018 ± 13 Ma (n = 10, MSWD = 0.02) was

obtained from these same ten grains (Figure 6d). This age is interpreted as the magmatic protolith age.

In summary, all the zircons separated from mafic rock samples in northern Liaoning of the northern margin of the NCC record four distinct age groups including the first basalt (~2209 Ma (D1918)), the second diabase (~2154 Ma (D1917)), the third gabbro (~2063 Ma (D1919), and the forth amphibolite (~2018 Ma (D2012)), which represent the emplacement ages for the mafic rocks, respectively.

4.2. Major and Trace Element Geochemistry

The average SiO_2 content of the first three periods of mafic rocks is 49.27–50.33 wt%, while the fourth amphibolite has a lower average SiO_2 content (46.39 wt%). The Al_2O_3 content is moderate (13.22–14.86 wt%). The total alkali content (K_2O + Na_2O) is moderate, with the lowest being 2.95 wt% in the first basalt and ranging from 3.93 to 5.08 wt% in the other three stages of mafic rocks. On the TAS diagram (Figure 7a), most of the samples belong to the gabbro, and on the R1-R2 diagram (Figure 7b), they fall within the gabbro and olivine-gabbro area. The K_2O content of samples is very variable, with average values of 0.94 wt%, 0.42 wt%, 1.73 wt%, and 1.32 wt%, respectively. On the SiO_2-K_2O diagram, the samples belong to the calc-alkaline to high-K calc-alkaline series (Figure 7c), and Ta/Yb vs. Ce/Yb ratios allow an allocation to the calc-alkaline series (Figure 7d). The average Fe_2O_3 content of the samples is 2.13–3.50 wt%, with a high average FeO content of 9.41–11.90 wt%, an average MgO content of 6.17–7.50 wt%, and a low average content of TiO_2 (1.61–2.39 wt%) and MnO (0.17–0.21 wt%). $Mg^{\#}$ is low, ranging from 43.32 to 52.02, which is much lower than that of primary basaltic rocks ($Mg^{\#}$ = 70 [50]). The first basalt and the fourth amphibolite have a relatively high CaO content (9.52–10.00 wt%) and low P_2O_5 content (0.18–0.19 wt%), while the other two periods of mafic rocks have a relatively low CaO content (6.90–7.17 wt%) and high P_2O_5 content (0.25–0.39 wt%).

There are differences in the characteristics of rare earth elements and trace elements in these mafic rocks. The total contents of rare earth elements (REEs) in the first basalt and the fourth amphibolite are low, with average contents of 83 μg/g and 86 μg/g, respectively. On the chondrite-normalized rare earth element (REE) diagram, they exhibit similar characteristics to ocean island basalt (OIB), with a right-skewed smooth curve (Figure 8a), indicating an enrichment of light rare earth elements (LREEs) and a flat distribution pattern of heavy rare earth elements (HREEs). The differentiation between LREEs and HREEs is not significant, with an average $(La/Yb)_N$ value of 2.55–4.78 and a slight positive europium anomaly (Eu/Eu* = 0.98–1.06) (Figure 8a). In the primitive mantle-normalized trace element spider diagram, these two mafic rocks demonstrate similar characteristics, with an enrichment of large ion lithophile elements (LILEs) (Rb, Ba, K, etc.), depletion of high field strength elements (HFSEs) (Th, U, Nb, Ta, Zr, Ti, etc.), and negative anomalies of Sr and P, as well as slight positive anomalies of Zr and Hf (Figure 8b). The contents of Cr (with average contents of 106 μg/g and 129 μg/g), Co (with average contents of 51.2 μg/g and 48.4 μg/g), and Ni (with average contents of 73.6 μg/g and 98 μg/g) in these two mafic rocks are higher than normal mid-ocean ridge basalt (N-MORB).

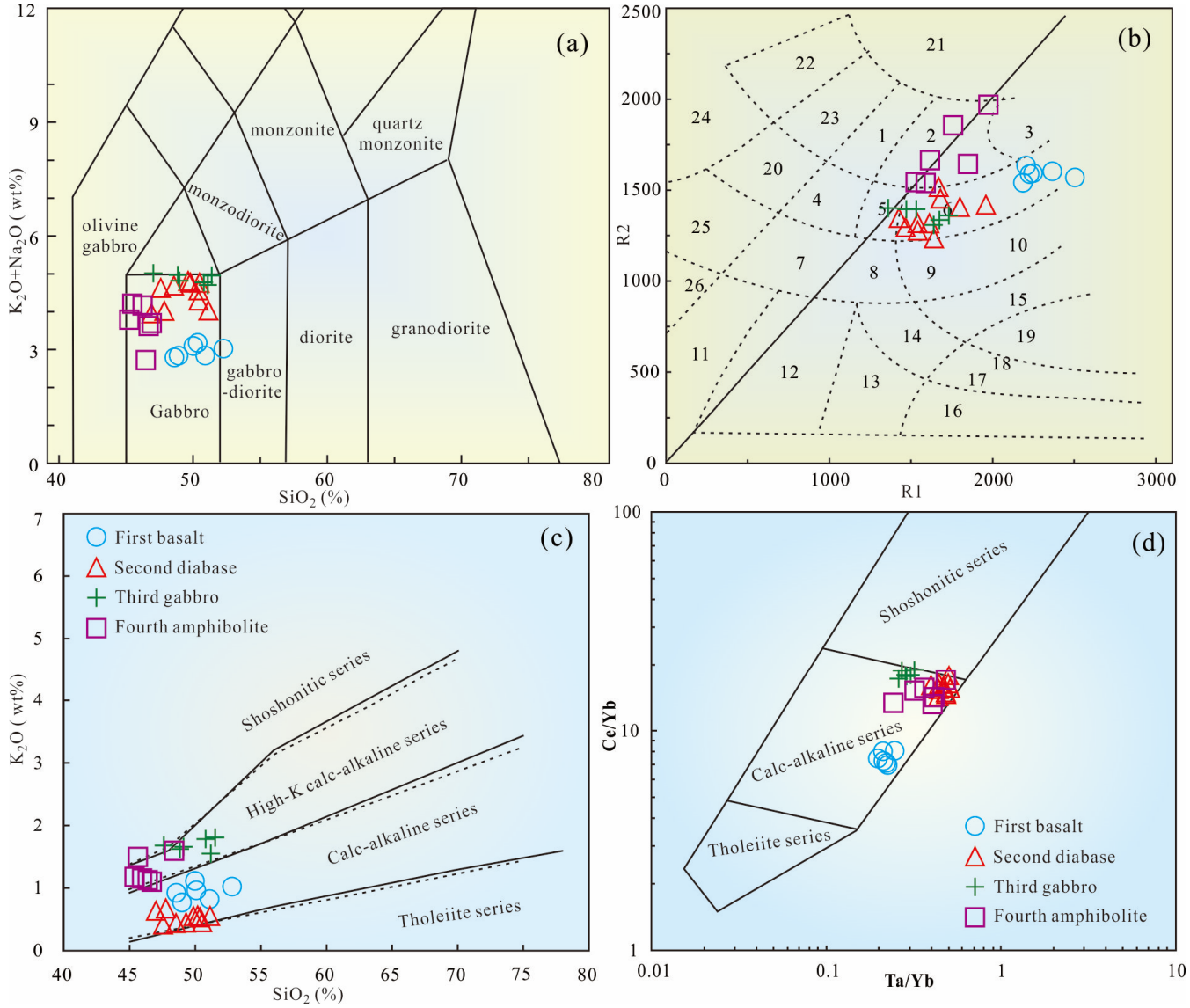

Figure 7. SiO_2 vs. total alkali (Na_2O + K_2O) ((**a**), after [51]), R1 vs. R2 ((**b**), after [52]), SiO_2-K_2O ((**c**), after [53]) and Ta/Yb vs. Ce/Yb ((**d**), after [54]) diagrams for mafic rocks from northern Liaoning. (**b**): 1—alkaline gabbro (alkaline basalt); 2—olivine gabbro (olivine basalt); 3—gabbro norite (tholeiite); 4—syenite gabbro (trachyte basalt); 5—monzonite gabbro (andesite coarse basalt); 6—gabbro (basalt); 7—trachyandesite (syenite); 8—monzonite (andesite); 9—monzodiorite (trachyte); 10—diorite (andesite); 11—nepheline syenite (trachyte phonolite); 12—syenite (trachyte); 13—quartz syenite (quartz trachyte); 14—quartz monzonite (quartz andesite); 15—tonalite (dacite); 16—alkaline granite (alkaline rhyolite); 17—syenogranite (rhyolite); 18—monzogranite (dacite rhyolite); 19—granodiorite (rhyolite dacite); 20—essenite aegirine gabbro; 21—peridotite (picrite); 22—nepheline (picrite nepheline); 23—qilieyan (basanite); 24—neonite (nepheline); 25—essenite; 26—nepheline syenite (phonolite).

The second diabase and the third gabbro show similar average REE contents, which are 119.28 μg/g and 121.41 μg/g, respectively, and are between OIB and N-MORB [55]. On the chondrite-normalized REE diagram, the samples show a right-skewed curve (Figure 8a), indicating an enrichment of LREEs and a flat pattern of HREEs. There is a slight differentiation between them, with average $(La/Yb)_N$ values of 5.44 and 7.32, respectively. The diabase shows a slight negative europium anomaly (Eu/Eu* = 0.72–0.88), while the gabbro exhibits a positive europium anomaly (Eu/Eu* = 1.31–1.37) (Figure 8a). In the primitive

mantle-normalized trace element spider diagram, the diabase is enriched in LILEs (Ba, etc.), relatively depleted in Rb and HFSEs (Th, U, Nb, Ta, Zr, Hf, Ti, etc.), and shows slight positive anomalies of K, Sr, and P, and Eu shows negative anomalies (Figure 8b); the gabbro shows the enrichment of LILEs (Rb, Ba, K), depletion of HFSEs (Th, U, Nb, Ta, Zr, Hf, etc.), and a positive anomaly of Eu (Figure 8b). The contents of Cr (with average contents of 123 μg/g and 113 μg/g), Co (with average contents of 46.8 μg/g and 62.7 μg/g), and Ni (with average contents of 71.4 μg/g and 74.0 μg/g) in these two mafic rocks are slightly higher than N-MORB.

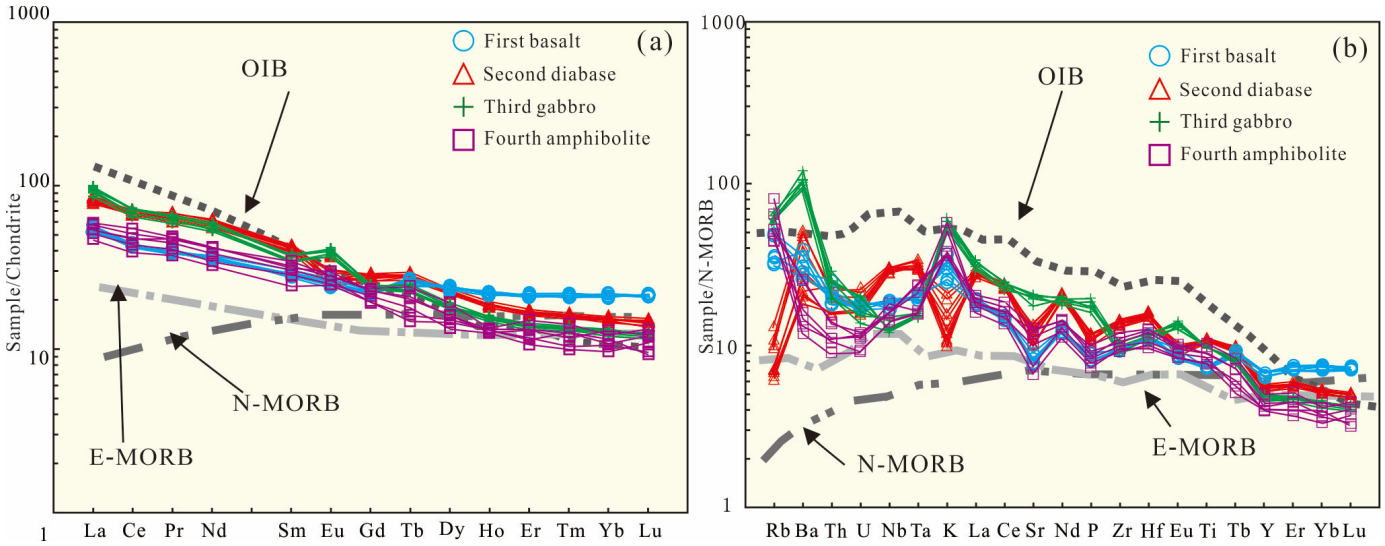

Figure 8. Chondrite-normalized rare earth element patterns (**a**) and primitive mantle-normalized trace element spider diagram (**b**) for the mafic rocks from northern Liaoning. (The values of chondrite and primitive mantle are from [55]).

5. Discussion

5.1. The Geochronological Significance of Mafic Rocks

5.1.1. Constraints on the Age of Proterozoic Strata in Northern Liaoning

The Proterozoic strata, exposed in northern Liaoning, are placed in the Changcheng, Jixian, and Nanhua System of the Meso-Neoproterozoic, according to the comparison of rock assemblage with the Proterozoic strata in western Liaoning [33]. However, after field investigation, this suite of strata has certain differences from the strata of Mesoproterozoic in western Liaoning. The Proterozoic strata in northern Liaoning has generally undergone metamorphism, with the lithology consisting of dolomite, meta-sandstone, meta-siltstone, and slate. These characteristics of rock composition and low-grade metamorphism are similar to those of the North Liaohe Groups and Laoling Groups in JLJB [56]. The mafic rocks studied in this paper intrude into the Kangzhuangzi Formation, Guanmenshan Formation, Tongjiajie Formation, and Hutouling Formation in northern Liaoning. They are considered to have formed in the Early Triassic according to whole-rock K–Ar dating results of 238.2 Ma [33].

However, the credibility of this chronology result is doubted: (1) In northern Liaoning, these mafic rocks have intruded into the earlier strata with objective contact metamorphic belts, rather than the Neoproterozoic strata (Figure 1b). (2) Partial pillow-shaped mafic rocks, associated with marble and dolomite, are in tectonic contact with the surrounding Permian granite (Figure 1c). (3) Metamorphism is widely developed in these mafic rocks. Pyroxene has undergone metamorphism into amphibole and carbonation or with brown amphibole reaction edges partially. Plagioclase has undergone epidotization, zoisitization, etc. Olivine has intensely metamorphosed into microscale biotite, magnetite, etc. Hornblende has undergone chloritization. Some mafic rocks have metamorphosed into amphibolite (Figure 2k,l).

Four zircon U-Pb ages have been obtained from the mafic rocks in northern Liaoning, ~2209 Ma, ~2154 Ma, ~2055 Ma, and ~2018 Ma, recording four periods of mafic magmatic activity. These results indicate that the emplacement age of the mafic rocks is the Paleoproterozoic rather than the Early Triassic, which means the intruded strata by, or associated with, the mafic rocks were formed in the Paleoproterozoic or earlier. Combined with the unconformity of overlying the Neoproterozoic granite, the formation age of these strata should be corrected to Paleoproterozoic.

5.1.2. Paleoproterozoic Mafic Magmatic Events in the Eastern Segment of the NCC

In this study, four episodes of mafic magmatic activities have been identified in northern Liaoning. Meanwhile, a 2118 Ma metamorphic basic dyke has recently been reported in the Qingyuan area [30]. The magmatic activities of mafic rocks in the eastern segment of the NCC are primarily concentrated in the JLBT and persist from approximately 2209 Ma to around 1820 Ma. The rock assemblage with this activity includes basalt, diabase, gabbro, and amphibolite, which are found as intrusions, sills, dykes, or strata interlayers coexisting with Paleoproterozoic meta-sedimentary and metamorphic rocks. Based on previous studies and new data obtained in this study, a chronological framework for these Paleoproterozoic mafic magmatic activities in the eastern segment of the NCC has been established. This framework provides a timeline of when these events occurred, helping scientists understand the sequence of geological processes during this time (Figure 8, Table 4).

Table 4. Summary of geochronological data of Paleoproterozoic mafic rocks in the eastern segment of the NCC.

No.	Sample	Lithology	U-Pb Age (Ma)	Location	Analytical Method	References
1	D021	Amphibolite	1952 ± 38	Zhujiagou	Zircon (LA-ICPMS)	[17]
2	D019	Amphibolite	2024 ± 33	124°58′14.9″, 40°47′22.5″	Zircon (LA-ICPMS)	[18]
3	D014	Amphibolite	2053 ± 34	124°55′53″, 40°39′13″	Zircon (LA-ICPMS)	[18]
4	D018	Amphibolite	2130 ± 19	124°58′43.8″, 40°47′12.8″	Zircon (LA-ICPMS)	[18]
5	HLY-3	Pillow basalt	1928 ± 16	Helan Town	Zircon (LA-ICPMS)	[19]
6	D15054	Amphibolite	1985 ± 31	Helan Town	Zircon (LA-ICPMS)	[19]
7	D1423-1	Amphibolite	2079 ± 21		Zircon (LA-ICPMS)	[19]
8	D1488-1	Amphibolite	2145 ± 19		Zircon (LA-ICPMS)	[19]
9	TWD15003	Meta-diabase	1821 ± 78	Lianshanguan Town	Zircon (LA-ICPMS)	[20]
10	TWD15008	Meta-diabase	2010 ± 27	Helan Town	Zircon (LA-ICPMS)	[20]
11	A1102	Meta-gabbro	2110 ± 31	Qianshan Town	Zircon (SHRIMP)	[57]
12	D1002-B1	Amphibolite	1995 ± 13	Huanghuadianzi Town	Zircon (LA-ICPMS)	[58]
13	D4034-B1	Amphibolite	2150 ± 21	Huanghuadianzi Town	Zircon (LA-ICPMS)	[58]
14		Gabbro	1880 ± 6		LA-ICP-MS	[59]
15		Amphibolite	1886 ± 26	Helan Town	LA-MC-ICP-MS	[59]
16		Gabbro	1914 ± 40	Helan Town	LA-MC-ICP-MS	[59]
17	SJZ07-2.1	Amphibolite	2167 ± 31	Sanjiazi Town	Zircon (LA-ICPMS)	[60]
18	DZ74-1	Meta-gabbro	2144 ± 16	Bahui Town	Zircon (LA-ICPMS)	[10]
19	DZ85-1	Meta-gabbro	2157 ± 17	Helan Town	Zircon (LA-ICPMS)	[10]
20	DZ73-1	Meta-gabbro	2159 ± 12	Helan Town	Zircon (LA-ICPMS)	[10]
21	DZ91-1	Meta-diabase	2161 ± 12	Mafeng Town	Zircon (LA-ICPMS)	[10]
22	DZ78-1	Amphibolite	2161 ± 45	Helan Town	Zircon (LA-ICPMS)	[10]
23	DZ40-2	Amphibolite	2159 ± 28	Fengcheng	Zircon (LA-ICPMS)	[11]
24	NLX02-4	Amphibolite	2163 ± 22	Helan Town	Zircon (SHRIMP)	[61]
25	09LG29	Gabbro	1828 ± 13	Helan Town	Zircon (SHRIMP)	[62]

Table 4. *Cont.*

No.	Sample	Lithology	U-Pb Age (Ma)	Location	Analytical Method	References
26	09LG28	Meta-mafic rock	1875 ± 28	Helan Town	Zircon (SHRIMP)	[62]
27	598XLLZ2	Meta-gabbro	2115 ± 13	Qianshan Town	Zircon (CAMECA)	[63]
28	598XLLZ2	Meta-gabbro	2115 ± 3	Qianshan Town	Baddeleyite (CAMECA)	[63]
29	SJZ07-5	Amphibolite	2054–2061	Sanjiazi Town	Zircon (LA-ICPMS)	[13]
30	16KD55-1-1	Amphibolite	2063 ± 23	Sanjiazi Town	Zircon (LA-ICPMS)	[13]
31	D2066-11	Amphibolite	2083 ± 13	Helan Town	Zircon (LA-ICPMS)	[13]
32	SJZ11-1	Amphibolite	2119 ± 19	Sanjiazi Town	Zircon (LA-ICPMS)	[13]
33	D1009-5	Meta-diabase	2100 ± 12	Helan Town	Zircon (LA-ICPMS)	[14]
34	D1009-7	Meta-diabase	2110 ± 23	Helan Town	Zircon (LA-ICPMS)	[14]
35	D1002-2	Meta-diabase	2133 ± 14	Helan Town	Zircon (LA-ICPMS)	[14]
36	D5048-4	Amphibolite	2164 ± 6	Helan Town	Zircon (LA-ICPMS)	[14]
37	D9001-1	Meta-gabbro	2118.6 ± 6.3	Helan Town	Zircon (LA-ICPMS)	[13]
38	16KD68-1	Meta-gabbro	2188.2 ± 8.5	Helan Town	Zircon (LA-ICPMS)	[13]
39	HP-9	Meta-mafic vein	2157 ± 21	Hupiyu Pluton	Zircon (LA-ICPMS)	[64]
40	DD24-1	Amphibolite	2059 ± 22	Mafeng Town	Zircon (LA-ICPMS)	[65]
41	YK12-1-4	Gabbro	2125 ± 6	Pailou Town	Zircon (LA-ICPMS)	[27]
42		Gabbro	2113 ± 15	Longchang Town	Zircon (LA-ICPMS)	[66]
43	15Q18	Metabasic dykes	2118 ± 18	124°56.57′, 42°12.66′	Zircon (LA-ICPMS)	[30]
44	D1917	basalt	2154 ± 15	125°57′05.27″, 41°21′16.88″	Zircon (LA-ICPMS)	This study
45	D1918	Diabase	2209 ± 12	124°12′36.40″, 42°05′01.27″	Zircon (LA-ICPMS)	This study
46	D1919	Gabbro	2063 ± 7	124°13′57.47″, 42°14′18.33″	Zircon (LA-ICPMS)	This study
47	D2012	Amphibolite	2018 ± 13	124°51′44.51″, 42°19′09.73″	Zircon (LA-ICPMS)	This study

In the eastern segment of the NCC, the Paleoproterozoic mafic rocks underwent four events of magmatism: The period from 2210 to 2100 Ma was marked by an especially intense activity of mafic magmatism. This mafic magmatic event started around 2209 Ma and persisted until 2100 Ma, with two significant peaks occurring at approximately 2162 Ma and 2108 Ma, respectively. The geological implications of this phenomenon suggest the potential onset and continuous development of ocean opening processes, commencing around 2209 Ma and extending until 2100 Ma when the ocean basin reached its maximum extent. From 2100 to 2000 Ma, the mafic magmatic activity gradually decreased, possibly indicating the onset of subduction and reduced basaltic magma activity in a compressional tectonic setting. Occasional mafic magmatic activity was observed from 2000 to 1900 Ma, which may be associated with a continent–continent collision and crustal thickening after 2000 Ma, resulting in reduced magmatic activity. After 1900 Ma, there was an increase in mafic magmatic activities. This could be attributed to the post-orogenic extensional phase. In this tensional tectonic setting, a certain scale of mafic magmatism occurred. However, due to the thicker crust at this time compared to earlier periods, the intensity of mafic magmatism during this stage was not as strong as that observed in the initial phase (Figure 9, Table 4).

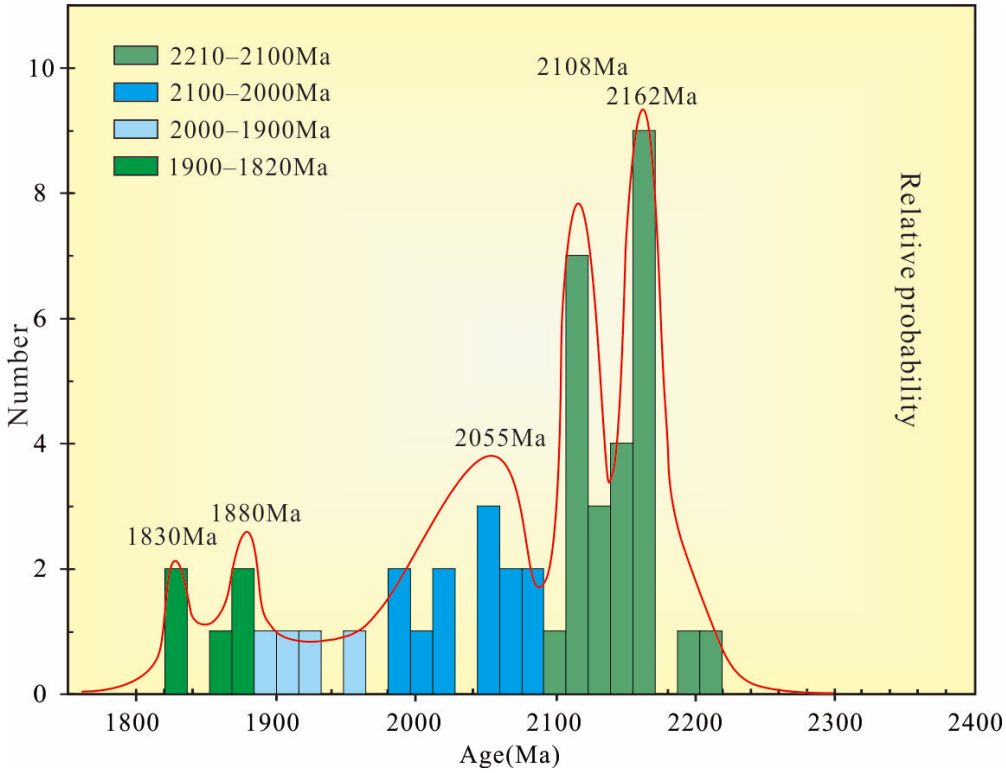

Figure 9. Age histogram of mafic rocks from the eastern segment of the NCC.

5.2. Source Characteristics and Genesis of the Paleoproterozoic Mafic Rocks

The ratio of some incompatible elements is stable during partial melting and fractional crystallization processes, which can largely reflect the characteristics of the source. For example, since Nb and Ta have similar valence states and ionic radii, their ratios are also comparable in igneous rocks from the same source. Similarly, Zr and Hf have similar valence states, ionic radii, and distribution coefficients in various minerals, so similar ratios and trends can be observed in rocks derived from the same origin. The ratios of Nb/Ta, Nb/La, Ta/Th, Ce/Pb, La/Pb, Nb/U, Zr/Nb, and Zr/Hf in the four periods of mafic rocks all show differences (Table 3), indicating that they come from different sources. These mafic rocks have undergone medium- to high-grade metamorphism and later experienced alteration processes such as sericitization, chloritization, and epidotization. During the process, highly active elements may migrate due to changing conditions, while REEs and HFSEs remain stable [67]. These elements are used to analyze and discuss the magma series, genesis, and source characteristics of metamorphic rocks [67].

Generally, mafic rocks originate from the mantle source [68]. The Paleoproterozoic mafic rocks are characterized by the enrichment of LREEs and LILEs, depletion of HREEs and HFSEs such as Nb, Ta, Ti, and Zr, and a slight negative or positive Eu anomaly, indicating characteristics of a mantle source [68]. The REE and trace element patterns of the Paleoproterozoic mafic rocks are different from N-MORB and E-MORB, but similar to OIB (Figure 8a,b), suggesting their origin from the lithospheric mantle rather than the asthenospheric mantle [68]. On the Nb/Th-Zr/Nb diagram, the first basalt is located between the primitive mantle, enriched mantle, and recycled slab, while the second diabase and fourth amphibolite are located at the transitional zone between the primitive mantle and recycled subduction slab, and the third gabbro is relatively close to the enriched mantle (Figure 10a). This indicates that the sources of these mafic rocks are transitional mantle.

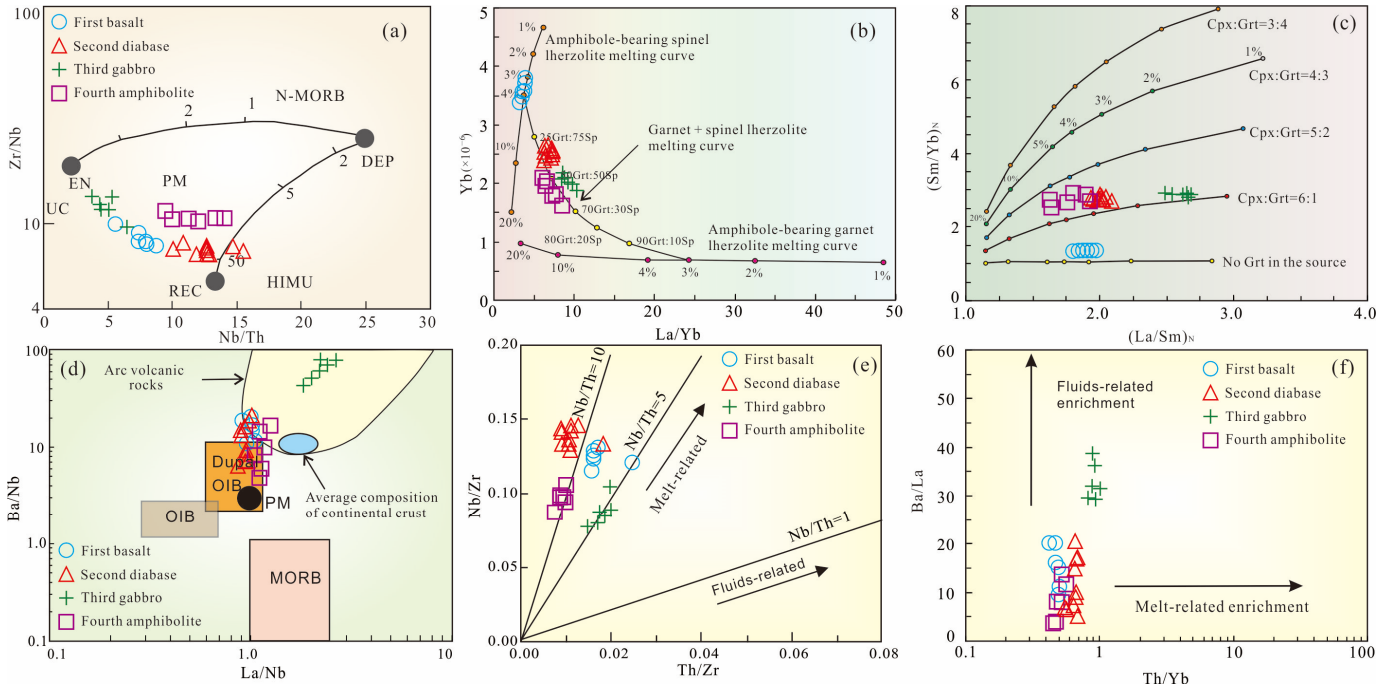

Figure 10. Source characteristics of the Triassic gabbro from the Kaiyuan Area. (**a**) After [69], DEP—depleted mantle, EN—enriched mantle, N-MORB—normal mid-ocean ridge basalt, PM—primitive mantle, REC—recycled plate, UC—upper crust. (**b**,**c**) After [70], Grt—garnet, SP—spinel. (**c**) Cpx—clinopyroxene. (**d**) After [71]. (**e**,**f**) After [72].

Due to the similar distribution coefficients, trace elements are difficult to fractionate during partial melting or fractional crystallization; they are usually used to reflect the nature of the parent magma in the magma source [70]. The first basalt shows flat patterns for REEs, with a low LREE/HREE ratio, indicating that there may be no residual garnet in the source area (Figure 10b,c). On the La/Yb-Yb diagram, it is located at the 3–4% melting position of the Amphibole-bearing spinel lherzolite melting curve (Figure 10b), indicating the presence of residual amphibole and spinel in the magma source. The other stages of mafic rocks show similar patterns of enrichment in LREEs, relatively flat patterns of HREEs, high LREE/HREE ratios, and low Yb contents, indicating the presence of residual garnet in the source (Figure 10b,c). On the La/Yb-Yb diagram, they are located near the Garnet spinel lherzolite melting curve (Figure 10b), indicating the residual garnet and spinel in the magma source. The garnet to spinel ratio of the diabase is between 50:50 and 25:75, and the ratio of the gabbro and amphibolite is between 50:50 and 70:30 (Figure 10b). Differing from the partial melting of spinel lherzolite, during the partial melting process of different proportions of clinopyroxene and garnet, the properties of La/Sm and Sm/Yb show different characteristics, with Sm/Yb not changing with the decrease in La/Sm [73]. On the $(La/Sm)_N$-$(Sm/Yb)_N$ diagram (Figure 10c), consistent with the above conclusion, there is no garnet in the source, and the first basalt is the product of 3%–4% melting of amphibole-bearing spinel lherzolite. The other three stages of mafic rocks are products of partial melting of garnet–spinel lherzolite with a ratio of clinopyroxene to garnet of 6:1 to 5:2, only with different degrees of partial melting (Figure 10c [74]). The diabase, gabbro, and amphibolite show partial melting degrees of about 3%, 1%–2%, and 3%–5%, respectively (Figure 10c). All mafic rocks show negative Sr anomalies (Figure 10b), indicating the possible residual plagioclase in the source.

The mafic rocks exhibit similar enrichments in LREEs and LILEs such as Rb, Ba, and K, as well as depletions in HFSEs such as Nb, Ta, Zr, Hf, Ti, and P. In the La/Nb-Ba/Nb diagram (Figure 10d), the third gabbro falls within the area of island arc volcanic rocks, while the other mafic rocks fall within the transitional zone between Dupal OIB and arc

volcanic rocks. This could be related to the introduction of fluids or involvement of mantle components, indicating that metasomatic processes occurred in the source [75]. Thus, is the metasomatism caused by melts or fluids? The mafic rocks show high contents of Cr (average content of 106 μg/g, 123 μg/g, 113 μg/g, and 129 μg/g), Co (average content of 51.2 μg/g, 46.8 μg/g, 62.7 μg/g, and 48.4 μg/g), and Ni (average content of 73.6 μg/g, 71.4 μg/g, 74.0 μg/g, and 98 μg/g) compared to N-MORB, indicating that their source has undergone melt metasomatism, which is consistent with the trends shown in the Th/Zr-Nb/Zr diagram (Figure 10e). When the mantle-derived magma interacts with crustal material on the subducting plate and subducted oceanic crust, the magma generally exhibits low Na_2O, P_2O_5, and TiO_2 contents, positive anomalies of Nb, Ta, and Ti [76], or low Ce/Th (≈8), low Ba/Th (≈111), and obvious negative Ce anomaly [77]. The geochemical characteristics of these four episodes of mafic rocks are as follows: The first basalt exhibits a low Ce/Th (14.32), low Ba/Th (114.74), low Na_2O, P_2O_5, and TiO_2 contents, negative anomalies of Nb, Ta, and Ti (Figure 8b), and a slight negative Ce anomaly (average Ce/Ce* = 0.94). The second diabase exhibits high Na_2O, P_2O_5, and TiO_2 contents and positive anomalies of Nb, Ta, and Ti (Figure 8b), with low Ba/Th (114.74) but high Ce/Th (24.47), and a slightly negative Ce anomaly (average Ce/Ce* = 0.93). The third gabbro exhibits high Na_2O, P_2O_5, and TiO_2 contents, low Ce/Th (14.32), negative anomalies of Nb and Ta, no anomaly in Ti (Figure 8b), high Ba/Th (371.73), high Ce/Th (21.33), and a slightly negative Ce anomaly (average Ce/Ce* = 0.91). The fourth amphibolite exhibits a low Ba/Th (110.08) and a positive anomaly in Ti, but low Na_2O, P_2O_5, and TiO_2 contents, negative anomalies of Nb and Ta (Figure 8b), high Ce/Th (29.47), and a slightly negative Ce anomaly (average Ce/Ce* = 0.97). These characteristics indicate that all four stages of mafic rocks have undergone dual metasomatism by both fluid and melt, which is consistent with the trends shown in the Th/Zr-Nb/Zr and Th/Yb-Ba/La diagrams (Figure 10e,f). The third gabbro has undergone greater fluid metasomatism, while the others are mainly influenced by melt metasomatism.

Generally, mantle-derived magma may undergo assimilation and contamination with crustal materials during its ascent and emplacement. The geochemical data of the mafic rocks show moderate potassium and alkali contents (Figure 7c), low $Mg^{\#}$ ($Mg^{\#}$ = 43.32–52.02), enrichment in LILEs (Rb, Ba, K, etc.), and depletion in HFSEs (Nb, Ta, Zr, etc.). These characteristics suggest that the magma may have undergone contamination by crustal materials [78]. The Nb/Ta (average values of 15.63, 16.53, 15.01, and 15.74) and Zr/Hf (average values of 30.07, 31.88, 31.04, and 33.53) of the mafic rocks are similar to the values of the continental crust in eastern China (Nb/Ta = 15.38, Zr/Hf = 35.56, according to [79]), and lower than those of mid-ocean ridge basalts (MORB) and primitive mantle (Nb/Ta = 17.7, Zr/Hf = 36.1 [55]), indicating the influence of crustal contamination on the mafic magmas. The La/Sm is often used to reflect the degree of crustal contamination [80]. A higher La/Sm ratio often suggests a greater influence from crustal components, while a lower ratio may indicate a more pristine mantle signature [80]. The average La/Sm ratios of the four episodes of mafic rocks are 2.95, 3.11, 4.03, and 2.75, respectively, indicating the incorporation of continental crustal material during magma ascent. The intensity of crustal contamination is highest in the third gabbro, followed by the first basalt and second diabase, and weakest in the fourth amphibolite.

In conclusion, the Paleoproterozoic mafic rocks originated from a transitional mantle source. The first basalt, containing residual hornblende and spinel in the source, is the product of 3%–4% partial melting of amphibole-bearing spinel lherzolite. The source of the other three stages of mafic rocks contains residual garnet and spinel, and experienced partial melting of garnet–spinel lherzolite with a clinopyroxene to garnet ratio ranging from 6:1 to 5:2. The garnet to spinel ratios in these three mafic rocks range from 50:50 to 25:75 and 50:50 to 70:30, with partial melting degrees of 3%, 1%–2%, and 3%–5%, respectively. During the ascent and emplacement of all mafic magmas, they were contaminated by crustal material and incorporated continental crustal material.

5.3. Tectonic Setting of Paleoproterozoic Mafic Rocks

Mafic rocks formed in various tectonic settings show different TiO_2 contents [81]. Island arc basalt (IAB) typically contains the lowest TiO_2 content, around 0.98 wt% [81]. MORB contains a TiO_2 content of 1.5 wt%, while OIB contains the highest TiO_2 content at 2.63 wt% [81]. Within-plate basalts (WPB), on the other hand, show higher TiO_2 contents ranging from 2.23 wt% to 2.9 wt% [53]. In terms of trace element abundances, WPB generally show higher Nb and Ta contents, ranging from 13 to 84 μg/g and 0.73 to 5.9 μg/g, respectively. IAB, in contrast, exhibits very low Nb and Ta contents, ranging from 1.7 to 2.7 μg/g and 0.1 to 0.18 μg/g, respectively [53]. According to Condie's (1989) study on element ratios in different tectonic settings of basaltic rocks, WPB and MORB are enriched in TiO_2 and HFSEs. The element ratio shows the following characteristics: Nb/La > 0.8, Ti/Y > 350, Ti/V > 30, Hf/Ta < 5, La/Ta < 15, and Th/Ta < 3 [53,82]. On the contrary, it is similar to IAB on the active continental margin.

In this study, the third gabbro exhibits high TiO_2, Nb, and Ta contents (averages of 2.17 wt%, 9.42 μg/g, and 0.63 μg/g, respectively), as well as high Ti/Y and Ti/V ratios (averages of 587 and 42.5, respectively). This may be attributed to the influence of melt contamination, resulting in excessively high TiO_2 contents. The average trace element ratios of Nb/La = 0.43, Hf/Ta = 5.57, La/Ta = 34.87, and Th/Ta = 3.19 indicate that it differs from WPB and MORB but shares similarities with continental arc basalts (CAB) [53,82]. The gabbro also exhibits characteristics of island arc volcanic rocks in the La/Nb-Ba/Nb diagram (Figure 10d). Furthermore, in the Hf/3-Th-Nb/16 triangular diagram and Nb/Yb-Th/Yb diagram, the gabbro falls within the continental arc region (Figure 11a,b). These characteristics suggest that the gabbro was formed in an island arc environment.

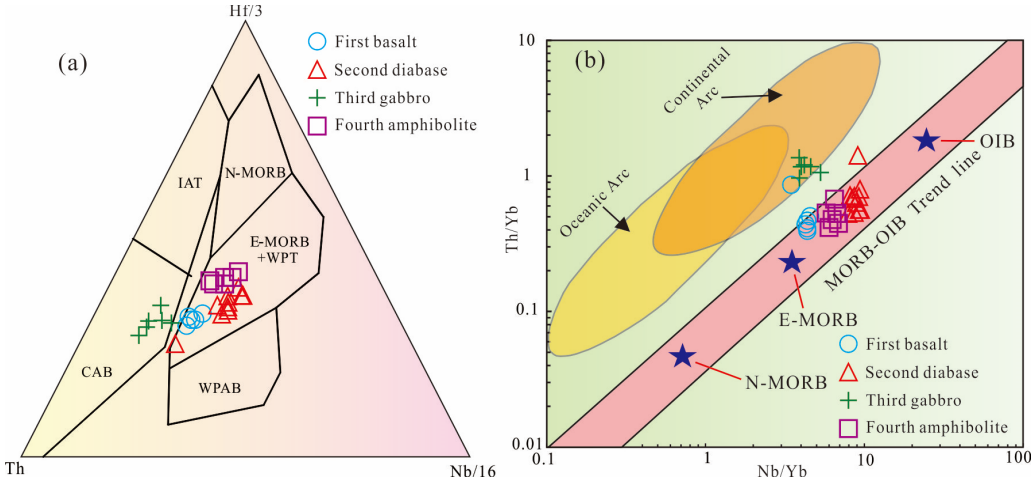

Figure 11. Identification diagram of tectonic setting for the mafic rocks from northern Liaoning. (**a**) Hf/3 versus Th versus Nb/16 (after [83]); (**b**) Nb/Yb versus Th/Yb diagram (after [83]).

The other three phases of mafic rocks show high TiO_2 (averages of 1.61 wt%, 2.39 wt%, 1.94 wt%), Nb (averages of 13 μg/g, 21 μg/g, 11.2 μg/g), and Ta (averages of 0.83 μg/g, 1.28 μg/g, 0.76 μg/g) contents. The average trace element ratios of Nb/La (averages of 1.01, 1.08, 0.89), Ti/Y (averages of 351, 558, 587), Ti/V (averages of 30.01, 39.5, 43.4), Hf/Ta (averages of 4.23, 3.78, 4.82), La/Ta (averages of 15.4, 15.3, 16.6), and Th/Ta (averages of 2.42, 1.42, 1.33) indicate that they are similar with WPB and MORB. They also share similar characteristics in the Hf/3-Th-Nb/16 triangular diagram (Figure 11a). The first basalt and the second diabase intrude into the limestone as sills, while the fourth amphibolite is surrounded by marble. These field features are similar to the rock assemblage of oceanic islands or seamounts. The geochemical characteristics of these three phases of mafic rocks are similar to OIB. In the La/Nb-Ba/Nb diagram, they mainly originate from the Dupal OIB and transition to arc volcanic rocks (Figure 10d), and in the Nb/Yb-Th/Yb diagram,

they fall on the MORB-OIB trend line, indicating that these three phases of mafic rocks were formed in an oceanic island environment (Figure 11b).

The formation mechanism of the Paleoproterozoic orogenic belt (JLJB) in the eastern segment of the NCC has been a subject of ongoing debate and differing interpretations among geologists [4,5,8,9,13–20,30,84]. One view suggests that it resulted from subduction and continental collision from the northern plate of the Longgang block, with the JLJB forming in an arc-back basin, and the northern margin of the NCC belonging to a continental margin sedimentary environment [4,5]. Previous studies on high-pressure granulite metamorphic rocks in the northern margin of the NCC proposed the existence of an east–west striking Paleoproterozoic orogenic belt (IMNHB), which may have formed during the assembly of the Columbia supercontinent, influenced by the closure, disappearance, and collision of the northern ocean of the NCC [4,5,8,9]. It is believed that this orogenic belt extended from Hebei to northern Liaoning [9]. The Paleoproterozoic mafic magmatic events and metamorphism in the Hebei–Northern Liaoning area also support the existence of this orogenic belt [30,84]. The mafic rocks identified in this study were formed in an oceanic island and island arc tectonic setting, indicating the existence of subduction, and the extinction of ocean and continent–continent collision in the north of the Longgang Block during the Paleoproterozoic, which is consistent with Kusky's viewpoint.

However, in recent years, according to regional geological investigations and studies on magmatic rocks, and metamorphism and sedimentary rocks, more and more scholars believe that the JLJB is a locally ordered and globally disordered mélange, and the formation of JLJB is related to northward subduction of the Nangrim Block in the south towards to the Longgang Block in the north [1,2,13–20]. The genetic models of JLJB in the subduction environment can be divided into two types: the continent–arc–continent collision model [13–15,24–27] and the rift–subduction–collision cycle model [2,6,7,18–20,28,29].

The debate between these two views lies in whether the subduction occurred in the south or north of the Longgang Block. The geochronological framework of mafic magmatic activity in the eastern segment of the NCC shows that there were similar mafic magmatic activities in the northern and southern parts of the Longgang Block during the Paleoproterozoic. Therefore, the northern and southern parts of the Longgang Block may have been in two different tectonic domains in the Paleoproterozoic. This issue requires further research in the future.

6. Conclusions

(1) Zircon U-Pb ages (2209 ± 12 Ma, 2154 ± 15 Ma, 2063 ± 7 Ma, 2018 ± 13 Ma) and metamorphic ages (1835 ± 13 Ma) have been obtained from mafic rocks in northern Liaoning, which constrained the formation age of the Proterozoic strata to be Paleoproterozoic. Based on previous data, the Paleoproterozoic mafic magmatic activities in the eastern segment of the NCC can be classified into four stages: the most frequent activity occurred between 2210 and 2100 Ma, gradually decreased between 2100 and 2000 Ma, with occasional activities between 2000 and 1900 Ma, and increased activities after 1900 Ma.

(2) Geochemical characteristics reveal that the four stages of mafic rocks belong to the calc-alkaline series and originated from transitional mantle. During the process of magma ascent and emplacement, the magma underwent contamination by crustal materials. The first basalt contains residual hornblende and spinel in the source, and is a product of 3–4% partial melting of amphibole-bearing spinel lherzolite. The other mafic rocks contain residual garnet and spinel in the source, and experienced partial melting of garnet–spinel lherzolite with a clinopyroxene to garnet ratio ranging from 6:1 to 5:2. The proportions of garnet to spinel range from 25:75 to 70:30, and the degrees of partial melting are 3%, 1%–2%, and 3%–5%, respectively.

(3) Trace element data indicate that the third gabbro exhibits characteristics of continental island arc basalts, suggesting it was formed in an island arc environment. The other three stages of mafic rocks originated from the Dupal OIB and formed in an oceanic island environment. The identification of Paleoproterozoic magmatic and subsequent

metamorphic events in the mafic rocks from northern Liaoning, as well as the verification that the northern orogenic belt of the NCC extends to this region, suggests that the north of the Longgang Block may be under an oceanic subduction tectonic setting. JLJB was formed under the background of a northward subduction of the Nangrim Block or island arc in the south of the Longgang Block. Therefore, it is possible that the northern and southern parts of the Longgang block were located at different tectonic domains in the Paleoproterozoic.

Author Contributions: Conceptualization, J.C.; formal analysis, J.C., Y.T., B.L. and W.L.; investigation, J.C., Y.T., Z.G., B.L., C.Z. (Chen Zhao), W.L., C.Z. (Chao Zhang). and Y.W.; writing—original draft preparation, J.C. and B.L.; writing—review and editing, J.C. and B.L.; projection administration, Y.W. All authors have read and agreed to the published version of the manuscript.

Funding: This research was funded by the National Natural Science Foundation of China (U2244213) and the China Geological Survey (Grants DD20242929, DD20190042).

Data Availability Statement: The authors confirm that the data generated or analyzed during this study are provided in full within the published article.

Acknowledgments: We thank the editors and anonymous reviewers for their critical reviews and excellent suggestions that helped to improve this manuscript. We thank the staff of the Key laboratory of Mineral Resources Evaluation in Northeast Asia, Ministry of Natural Resources, for their advice and assistance during the zircon U-Pb dating by LA-ICP-MS. We also thank the Northeast China Supervision and Inspection Center of Mineral Resources, Ministry of Natural Resources, Shenyang, China, for their assistance in the major and trace element analysis.

Conflicts of Interest: Yi Tian, Zhonghui Gao, Weiwei Li were employed by the company Institute of Geology and Mineral resources of Liaoning Co., Ltd. The remaining authors declare that the research was conducted in the absence of any commercial or financial relationships that could be construed as a potential conflict of interest.

References

1. Zhao, G.C.; Sun, M.; Wilde, S.A.; Li, S.Z. Late Archean to Paleoproterozoic evolution of the North China Craton: Key issues revisited. *Precambrian Res.* **2005**, *136*, 177–202. [CrossRef]
2. Zhao, G.C.; Cawood, P.A.; Li, S.Z.; Wilde, S.A.; Sun, M.; Zhang, J.; He, Y.; Yin, C. Amalgamation of the North China Craton: Key issues and discussion. *Precambrian Res.* **2012**, *222–223*, 56–76. [CrossRef]
3. Faure, M.; Trap, P.; Lin, W.; Monié, P.; Bruguier, O. Polyorogenic Evolution of the Paleo-Proterozoic Trans-North China Belt: New Insights from the Lvliangshan-Hengshan-Wutaishan and Fuping Massifs. *Episodes* **2007**, *30*, 96–107. [CrossRef]
4. Kusky, T.M. Geophysical and geological tests of tectonic models of the North China Craton. *Gondwana Res.* **2011**, *20*, 26–35. [CrossRef]
5. Kusky, T.M.; Polat, A.; Windley, B.F.; Burke, K.C.; Dewey, J.F.; Kidd, W.S.F.; Maruyama, S.; Wang, J.P.; Deng, H.; Wang, Z.S.; et al. Insights into the tectonic evolution of the North China Craton through comparative tectonic analysis: A record of outward growth of Precambrian continents. *Earth-Sci. Rev.* **2016**, *162*, 387–432. [CrossRef]
6. Zhai, M.G.; Santosh, M. The early Precambrian odyssey of North China Craton: A synoptic overview. *Gondwana Res.* **2011**, *20*, 6–25. [CrossRef]
7. Zhai, M.G.; Santosh, M. Metallogeny of the North China Craton: Link with secular changes in the evolving Earth. *Gondwana Res.* **2013**, *24*, 275–297. [CrossRef]
8. Kusky, T.M.; Li, J.H. Paleoproterozoic tectonic evolution of the North China Craton. *J. Asian Earth Sci.* **2003**, *22*, 383–397. [CrossRef]
9. Kusky, T.M.; Li, J.H.; Santosh, M. The Paleoproterozoic North Hebei orogen: North China Craton's collisional suture with the Columbia supercontinent. *Gondwana Res.* **2007**, *12*, 4–28. [CrossRef]
10. Meng, E.; Liu, F.L.; Liu, P.H.; Liu, C.H.; Yang, H.; Wang, F.; Shi, J.R.; Cai, J. Petrogenesis and tectonic significance of Paleoproterozoic meta-mafic rocks from central Liaodong Peninsula, northeast China: Evidence from zircon U-Pb dating and in situ Lu-Hf isotopes, and whole-rock geochemistry. *Precambrian Res.* **2014**, *247*, 92–109. [CrossRef]
11. Meng, E.; Wang, C.Y.; Li, Y.G.; Li, Z.; Yang, H.; Cai, J.; Ji, L.; Jin, M.Q. Zircon U-Pb-Hf isotopic and whole-rock geochemical studies of Paleoproterozoic metasedimentary rocks in the northern segment of the Jiao-Liao-Ji Belt, China: Implications for provenance and regional tectonic evolution. *Precambrian Res.* **2017**, *298*, 472–489. [CrossRef]
12. Liu, J.H.; Liu, F.L.; Ding, Z.J.; Liu, P.H.; Guo, C.L.; Wang, F. Geochronology, petrogenesis and tectonic implications of Paleoproterozoic granitoid rocks in the Jiaobei Terrane, North China Craton. *Precambrian Res.* **2014**, *255*, 685–698. [CrossRef]
13. Xu, W.; Liu, F.L.; Santosh, M.; Liu, P.H.; Tian, Z.H.; Dong, Y.S. Constraints of mafic rocks on a Paleoproterozoic back-arc in the Jiao-Liao-Ji Belt, North China Craton. *J. Asian Earth Sci.* **2018**, *166*, 195–209. [CrossRef]

14. Xu, W.; Liu, F.L.; Tian, Z.H.; Liu, L.S.; Ji, L.; Dong, Y.S. Source and petrogenesis of Paleoproterozoic meta-mafic rocks intruding into the North Liaohe Group: Implications for back-arc extension prior to the formation of the Jiao-Liao-Ji Belt, North China Craton. *Precambrian Res.* **2018**, *307*, 66–81. [CrossRef]
15. Xu, W.; Liu, F.L. Geochronological and geochemical insights into the tectonic evolution of the Paleoproterozoic Jiao-Liao-Ji Belt, Sino-Korean Craton. *Earth-Sci. Rev.* **2019**, *193*, 162–198. [CrossRef]
16. Chen, J.S.; Xing, D.H.; Liu, M.; Li, B.; Yang, H.; Tian, D.X.; Yang, F.; Wang, Y. Zircon U–Pb chronology and geological significance of felsic volcanic rocks in the Liaohe Group from the Liaoyang area, Liaoning Province. *Acta Petrol. Sin.* **2017**, *33*, 2792–2810. (In Chinese with English Abstract)
17. Chen, J.S.; Jiang, Z.Q.; Li, W.W.; Li, B.; Liu, M.; Yang, F.; Xing, D.H.; Wang, Y.; Tan, H.Y. The formation ages of the Langzishan and Lieryu formations in Lianshanguan area, Benxi, Liaoning province, and its geological significance. *Geol. Bull. China.* **2018**, *37*, 1693–1703. (In Chinese with English Abstract)
18. Chen, J.S.; Tian, D.X.; Xing, D.H.; Li, B.; Liu, M.; Yang, F.; Yang, Z.Z. Zircon U-Pb Geochronology and Its Geological Significance of the Basic Volcanic Rocks from the Li'eryu Formation, Liaohe Group in Kuandian Area. *Earth Sci.* **2020**, *45*, 3282–3294. (In Chinese with English Abstract)
19. Chen, J.S.; Li, W.W.; Xing, D.H.; Yang, Z.Z.; Tian, D.X.; Zhang, L.D.; Li, B.; Liu, M.; Yang, F. Zircon U-Pb geochronology of volcanic rocks from Gaojiayu Formation, Liaohe Group, Liaoning Province and its geological significance. *Earth Sci.* **2020**, *45*, 3934–3949. (In Chinese with English Abstract)
20. Chen, J.S.; Yang, Z.Z.; Tian, D.X.; Xing, D.H.; Zhang, L.D.; Yang, F.; Li, B.; Liu, M.; Shi, Y.; Zhang, C. Geochronological Framework of Paleoproterozoic Intrusive Rocks and Its Constraints on Tectonic Evolution of the Liao-Ji Belt, Sino-Korean Craton. *J. Earth Sci.* **2021**, *32*, 8–24. [CrossRef]
21. Zhang, Q.S. Early proterozoic tectonic styles and associated mineral deposits of the North China platform. *Precambrian Res.* **1988**, *39*, 1–29. [CrossRef]
22. Li, S.Z.; Zhao, G.C. SHRIMP U-Pb zircon geochronology of the Liaoji granitoids:constraints on the evolution of the Paleoproterozoic Jiao-Liao-Ji belt in the eastern block of the North China Craton. *Precambrian Res.* **2007**, *158*, 1–16. [CrossRef]
23. Wang, F.; Liu, F.L.; Liu, P.H.; Cai, J.; Schertl, H.P.; Ji, L.; Liu, L.S.; Tian, Z.H. In situ zircon U-Pb dating and whole-rock geochemistry of metasedimentary rocks from South Liaohe Group, Jiao-Liao-Ji orogenic belt: Constraints on the depositional and metamorphic ages, and implications for tectonic setting. *Precambrian Res.* **2017**, *303*, 764–780. [CrossRef]
24. Bai, J. *The Precambrian Geology and Pb-Zn Mineralization in the Northern Margin of North China Platform*; Geological Publishing House: Beijing, China, 1993; pp. 1–136. (In Chinese with English Abstract)
25. Faure, M.; Lin, W.; Monie, P.; Bruguier, O. Palaeoproterozoic arc magmatism and collision in Liaodong Peninsula (north-east China). *Terra Nova* **2004**, *16*, 75–80. [CrossRef]
26. Li, Z.; Chen, B. Geochronology and geochemistry of the Paleoproterozoic metabasalts from the Jiao-Liao-Ji Belt, North China Craton: Implications for petrogenesis and tectonic setting. *Precambrian Res.* **2014**, *255*, 653–667. [CrossRef]
27. Yuan, L.L.; Zhang, X.H.; Xue, F.H.; Han, C.M.; Chen, H.H.; Zhai, M.G. Two episodes of Paleoproterozoic mafic intrusions from Liaoning province, North China Craton: Petrogenesis and tectonic implications. *Precambrian Res.* **2015**, *264*, 119–139. [CrossRef]
28. Li, S.Z.; Zhao, G.C.; Santosh, M.; Liu, X.; Dai, L.M.; Suo, Y.H.; Tam, P.Y.; Song, M.C.; Wang, P.C. Paleoproterozoic structural evolution of the southern segment of the Jiao-Liao-Ji Belt, North China Craton. *Precambrian Res.* **2012**, *200–203*, 59–73. [CrossRef]
29. Zhao, G.C.; Zhai, M.G. Lithotectonic elements of Precambrian basement in the North China Cration: Review and tectonic implications. *Gondwana Res.* **2013**, *23*, 1207–1240. [CrossRef]
30. Duan, Z.Z.; Wei, C.J.; Li, Z. Metamorphic P-T paths and zircon U-Pb ages of Paleoproterozoic metabasic dykes in eastern Hebei and northern Liaoning: Implications for the tectonic evolution of the North China Craton. *Precambrian Res.* **2019**, *326*, 124–141. [CrossRef]
31. Wu, D.; Wei, C.J. Metamorphic evolution of two types of garnet amphibolite from the Qingyuan terrane, North China Craton: Insights from phase equilibria modelling and zircon dating. *Precambrian Res.* **2021**, *355*, 106091. [CrossRef]
32. Cui, R.Z.; Wei, C.J.; Duan, Z.Z. Two phases of granulite facies metamorphism during the Neoarchean and Paleoproterozoic in the Oingyuan terrane, North China Craton. *Acta Petrol. Sin.* **2023**, *39*, 2257–2278. (In Chinese with English Abstract) [CrossRef]
33. Bureau of Geology and Mineral Resource of Liaoning Province. *Regional Geology of Liaoning Province*; Geological Publishing House: Beijing, China, 2014; pp. 595–763. (In Chinese)
34. Zhao, G.C.; Cao, L.; Wilde, S.; Sun, M.; Choe, W.; Li, S.Z. Implications based on the first SHRIMP U–Pb zircon dating on Precambrian granitoid rocks in North Korea. *Earth Planet. Sci. Lett.* **2006**, *251*, 365–379. [CrossRef]
35. Li, Z.; Meng, E.; Wang, C.Y.; Li, Y.G. Early Precambrian tectonothermal events in the Southern Jilin Province, China: Implications for Neoarchean crustal evolution of the northeastern North China Craton. *Mineral. Petrol.* **2019**, *113*, 185–205. [CrossRef]
36. Li, Z.; Wei, C.J.; Chen, B.; Fu, B.; Gong, M.Y. Late Neoarchean reworking of the Mesoarchean crustal remnant in northern Liaoning, North China Craton: A U-Pb-Hf-O-Nd perspective. *Gondwana Res.* **2020**, *80*, 350–369. [CrossRef]
37. Peng, P.; Wang, C.; Wang, X.P.; Yang, S.Y. Qingyuan high-grade granite-greenstone terrain in the Eastern North China Craton: Root of a Neoarchaean arc. *Tectonophysics* **2015**, *662*, 7–21. [CrossRef]
38. Li, Z.; Wei, C.J. Two Types of Neoarchean basalts from Qingyuan greenstone belt, North China Craton: Petrogenesis and tectonic implications. *Precambrian Res.* **2017**, *292*, 175–193. [CrossRef]

39. Wan, Y.S.; Song, B.; Yang, C.; Liu, D.Y. Zircon SHRIMP U-Pb geochronology of Archaean rocks from the Fushun-Qingyuan area, Liaoning province and its geological significance. *Acta Geol. Sin.* **2005**, *79*, 78–87. (In Chinese with English Abstract)
40. Dickinson, J.E., Jr.; Hess, P.C. Zircon saturation in lunar basalts and granites. *Earth Planet. Sci. Lett.* **1982**, *57*, 336–344. [CrossRef]
41. Shao, T.; Xia, Y.; Ding, X.; Cai, Y.; Song, M. Zircon saturation in terrestrial basaltic melts and its geological implications. *Solid Earth Sci.* **2019**, *4*, 27–42. [CrossRef]
42. Bea, F.; Bortnikov, N.; Cambese, A.; Chakraborty, S.; Molina, J.F.; Montero, P.; Morales, I.; Silantiev, S.; Zinger, T. Zircon crystallization in low-Zr mafic magmas: Possible or impossible? *Chem. Geol.* **2022**, *602*, 120898. [CrossRef]
43. Wiedenbeck, M.; Allé, P.; Corfu, F.; Griffin, W.L.; Meier, M.; Oberli, F.; Quadt, A.; Roddick, J.C.; Spiegel, W. Three natural zircon standards for U-Th-Pb, Lu-Hf, trace element and REE analyses. *Geostand. Newsletter.* **1995**, *19*, 1–23. [CrossRef]
44. Ludwig, K.R. User's manual for isoplot 3.0: A geochronological toolkit for microsoft excel. *Berkeley Geochronol. Cent. Spec. Publ.* **2003**, *4*, 75.
45. Andersen, T. Correction of common Lead in U-Pb analyses that do not report ^{204}Pb. *Chem. Geol.* **2002**, *192*, 59–79. [CrossRef]
46. Belousova, E.; Griffin, W.; O'Reilly, S.Y.; Fisher, N. Igneous zircon: Trace element composition as an indicator of source rock type. *Contrib. Mineral. Petrol.* **2002**, *143*, 602–622. [CrossRef]
47. Hoskin, P.W.O.; Ireland, T.R. Rare earth element chemistry of zircon and its use as a provenance indicator. *Geology* **2000**, *28*, 627–630. [CrossRef]
48. Li, C.M. A review on the minerageny and situ microanalytical dating techniques of zircons. *Geol. Surv. Res.* **2009**, *33*, 161–174. (In Chinese with English Abstract)
49. Liu, D.Y.; Wilde, S.A.; Wan, Y.S.; Shiyan Wang, S.Y.; Valley, J.W.; Kita, N.; Dong, C.Y.; Xie, H.Q.; Yang, C.X.; Zhang, Y.X.; et al. Combined U-Pb, hafnium and oxygen isotope analysis of zircons from meta-igneous rocks in the southern North China Craton: Reveal multiple events in the Late Mesoarchean-Early Neoarchean. *Chem. Geol.* **2009**, *261*, 139–153. [CrossRef]
50. Dupuy, C.; Dostal, J. Trace element geochemistry of some continental tholeiites. *Earth Planet. Sci. Lett.* **1984**, *67*, 61–69. [CrossRef]
51. Middlemost, E.A.K. Naming materials in the magma/igneous rock system. *Earth-Sci. Rev.* **1994**, *37*, 215–224. [CrossRef]
52. De la Roche, H.; Leterrier, J.; Grandclaude, P.; Marchal, M. A classification of volcanic and plutonic rocks using R1R2-diagram and major-element analyses—Its relationships with current nomenclature. *Chem. Geol.* **1980**, *29*, 183–210. [CrossRef]
53. Peccerillo, A.; Taylor, S.R. Geochemistry of Eocene calc-alkaline volcanic rocks from the Kastamonu area, northern Turkey. *Contrib. Mineral. Petrol.* **1976**, *58*, 63–81. [CrossRef]
54. Pearce, J.A. Trace elements characteristic of lavas from destructive plate boundaries. Andesites. In *Thorpe R S. Orogenic Andesites and Related Rocks*; John Wiley & Sons: Chichester, UK, 1982; pp. 525–548.
55. Sun, S.S.; McDonough, W.F. Chemical and isotopic systematics of oceanic basalts: Implications for mantle composition and processes. *Geol. Soc. Lond. Spec. Publ.* **1989**, *42*, 313–345. [CrossRef]
56. Liu, F.L.; Liu, P.H.; Wang, F.; Liu, C.H.; Cai, J. Progresses and overviews of voluminous meta-sedimentary series within the Paleoproterozoic Jiao-Liao-Ji orogenic/mobile belt, North China Craton. *Acta Petrol. Sin.* **2015**, *31*, 2816–2846. (In Chinese with English Abstract)
57. Dong, C.Y.; Ma, M.Z.; Liu, S.J.; Xie, H.Q.; Liu, D.Y.; Li, X.M.; Wan, Y.S. Middle Paleoproterozoic crustal extensional regime in the North China Craton: New evidence from SHRIMP zircon U-Pb dating and whole-rock geochemistry of meta-gabbro in the Anshan-Gongchangling area. *Acta Petrol. Sin.* **2012**, *28*, 2785–2792. (In Chinese with English Abstract)
58. Gao, B.S.; Dong, Y.S.; Li, F.Q.; Wang, P.S.; Gan, Y.C.; Chen, M.S.; Tian, Z.H. Petrogenesis of the Li'eryu Formation of the South Liaohe Group in the Huanghuadian area, Liaodong Peninsula. *Acta Petrol. Sin.* **2017**, *33*, 2725–2742. (In Chinese with English Abstract)
59. Bureau of Geology and Mineral Resource of Liaoning Province. *Liaoning 1:50,000 Erpendianzi Regional Geological Survey*; Geological Publishing House: Beijing, China, 2019; 276p. (In Chinese)
60. Liu, P.H.; Cai, J.; Zou, L. Metamorphic P-T-t path and its geological implication of the Sanjiazi garnet amphibolites from the northern Liaodong Penisula, Jiao-Liao-Ji belt:Constraints on phase equilibria and zircon U-Pb dating. *Acta Petrol. Sin.* **2017**, *33*, 2649–2674. (In Chinese with English Abstract)
61. Qin, Y. Geochronological Constraints in the Tectonic Evolution of the Liao-Ji Paleoproterozoic Rift Zone. Ph.D. Thesis, Jilin University, Changchun, China, 2013; pp. 1–167. (In Chinese with English Abstract)
62. Wang, H.C.; Lu, S.N.; Chu, H.; Xiang, Z.Q.; Zhang, C.J.; Liu, H. Zircon U-Pb age and tectonic setting of meta-basalts of Liaohe Group in Helan area, Liaoyang, Liaoning Province. *J. Jilin Univ.* **2011**, *41*, 1322–1334. (In Chinese with English Abstract)
63. Wang, X.P.; Peng, P.; Wang, C.; Yang, S.Y. Petrogenesis of the 2115 Ma Haicheng mafic sills from the Eastern North China Craton: Implications for an intra-continental rifting. *Gondwana Res.* **2016**, *39*, 347–364. [CrossRef]
64. Yang, M.C.; Chen, B.; Yan, C. Petrogenesis of Paleoproterozoic gneissic granites from Jiao-Liao-Ji Belt of North China Craton and their tectonic implications. *J. Earth Sci. Environ.* **2015**, *37*, 31–51. (In Chinese with English Abstract)
65. Yu, J.J.; Yang, D.B.; Feng, H.; Lan, X. Chronology of amphibolite protolith in Haicheng of southern Liaoning: Evidence from LA-ICP-MS zircon U-Pb dating. *Glob. Geol.* **2007**, *26*, 391–396, 408. (In Chinese with English Abstract)
66. Zhao, Y.; Kou, L.L.; Zhang, P.; Bi, Z.W.; Li, D.T.; Chen, C. Characteristies of geochemistry and Hf isotope from meta-gabbro in Longchang area, Liaodong Peninsula: Implications on evolution of the Jiao-Liao-Ji Paleoproterozoic Orogenic Belt. *Earth Sci.* **2019**, *44*, 3333–3345. (In Chinese with English Abstract)

67. Kerrich, R.; Polat, A.; Wyman, D.; Hollings, P. Trace element systematics of Mg-, to Fe-tholeiitic basalt suites of the Superior Province: Implications for Archean mantle reservoirs and greenstone belt genesis. *Lithos* **1999**, *46*, 163–187. [CrossRef]
68. Sklyarov, E.V.; Gladkochub, D.P.; Mazukabzov, A.M.; Menshagin, Y.V.; Watanabe, T.; Pisarevsky, S.A. Neoproterozoic mafic dike swarms of the Sharyzhalgai metamorphic massif, southern Siberian Craton. *Precambrian Res.* **2003**, *122*, 359–376. [CrossRef]
69. Condie, K.C.; Frey, B.A.; Kerrich, R. The 1.75 Ga Iron King Volcanics in West Central Arizona: A remnant of an accreted Oceanic Plateau derived from a mantle plume with a deep depleted component. *Lithos* **2002**, *64*, 49–62. [CrossRef]
70. McKenzie, D.; O'Nions, R.K. Partial melt distribution from inversion of rare earth element concentrations. *J. Petrol.* **1991**, *32*, 1021–1091. [CrossRef]
71. Zhang, X.H.; Yuan, L.L.; Xue, F.H.; Zhang, Y.B. Contrasting Triassic ferroan granitoids from northwestern Liaoning, North China: Magmatic monitor of Mesozoic decratonization and a craton–orogen boundary. *Lithos* **2012**, *144–145*, 12–23. [CrossRef]
72. Woodhead, J.D.; Hergt, J.M.; Davidson, J.P.; Eggins, S.M. Hafnium isotope evidence for conservative element mobility during subduction zone process. *Earth Planet. Sci. Lett.* **2001**, *192*, 331–346. [CrossRef]
73. Aldanmaz, E.; Pearce, J.A.; Thirlwall, M.F.; Mitchell, J.G. Petrogenetic evolution of Late Cenozoic, post-collision volcanism in Western Anatolia, Turkey. *J. Volcanol. Geotherm. Res.* **2000**, *102*, 67–95. [CrossRef]
74. Jourdan, F.; Bertrand, H.; Schaerer, U.; Blichert-Toft, J.; Feraud, G.; Kampunzu, A.B. Major and trace element and Sr, Nd, Hf and Pb isotope compositions of the Karoo large igneous province, Botswana-Zimbabwe: Lithosphere vs mantle plume contribution. *Petrology* **2007**, *48*, 1043–1077. [CrossRef]
75. Sun, S.S.; Nesbitt, R.W. Geochemical regularities and genetic significance of ophiolitic basalts. *Geology* **1978**, *6*, 689–693. [CrossRef]
76. Sajona, F.G.; Maury, R.C.; Pubellier, M.; Leterrier, J.; Bellon, H.; Cotton, J. Magmatic source enrichment by slab-derived melts in a young post-collision setting, Central Mindanao (Philippines). *Lithos* **2000**, *54*, 173–206. [CrossRef]
77. Plank, T.; Langmuir, C.H. The chemical composition of subducting sediment and its consequences for the crust and mantle. *Chem. Geol.* **1998**, *145*, 325–394. [CrossRef]
78. Wu, F.Y.; Li, X.H.; Yang, J.H.; Zheng, Y.F. Discussions on the petrogenesis of granites. *Acta Petrol. Sin.* **2007**, *23*, 1217–1238. (In Chinese with English Abstract)
79. Chi, Q.H.; Yan, M.C. *Handbook of Elemental Abundance for Applied Geochemistry*; Geological Publishing House: Beijing, China, 2007; pp. 1–148. (In Chinese)
80. Zhang, Y.M.; Pei, X.Z.; Li, Z.C.; Li, R.B.; Liu, C.J.; Pei, L.; Chen, Y.X.; Wang, M. Zircon U-Pb geochronogy, geochemistry and its geological implication of the early indosinian basic complex in the Qinghai nanshan tectonic belt. *Earth Sci.* **2019**, *44*, 2461–2477. (In Chinese with English Abstract)
81. Wilson, M. *Igneous Petrogenesis: A global Tectonic Approach*; Unwin Hyman: London, UK, 1989; pp. 1–466.
82. Condie, K.C. Geochemical changes in baslts and andesites across the Archean? Proterozoic Boundary: Identification and significance. *Lithos* **1989**, *23*, 1–18. [CrossRef]
83. Pearce, J.A. A user's guide to basalt discrimination diagrams. In *Trace Element Geochemistry of Volcanic Rocks: Applications for Massive Sulphide Exploration*; Wyman, D.A., Ed.; Short Course Notes; Geological Association of Canada: St. John's, NF, Canada, 1996; Volume 12, pp. 79–113.
84. Duan, Z.Z.; Wei, C.J.; Qian, J.H. Metamorphic P-T paths and zircon U–Pb age data for the Paleoproterozoic metabasic dykes of high-pressure granulite facies from Eastern Hebei, North China Craton. *Precambrian Res.* **2015**, *271*, 295–310. [CrossRef]